Precambrian Research 342 (2020) 105677

Contents lists available at ScienceDirect

Precambrian Research

journal homepage: www.elsevier.com/locate/precamres

Discovery of kyanite in typically cordierite/sillimanite-bearing low- to medium-pressure pelitic granulites from the Jiaobei terrain, North China Craton

Yi Zou[a,b,d], Mingguo Zhai[a,c,*], Ross N. Mitchell[a], Lei Zhao[a], Ligang Zhou[b], Bo Liu[a], Yuquan Wang[a], Mengdie Chen[a]

[a] State Key Laboratory of Lithospheric Evolution, Institute of Geology and Geophysics, Chinese Academy of Sciences, Beijing 100029, China
[b] Key Laboratory of Mineral Resources, Institute of Geology and Geophysics, Chinese Academy of Sciences, Beijing 100029, China
[c] Key Laboratory of Computational Geodynamics, University of Chinese Academy of Sciences, Beijing 100029, China
[d] Innovation Academy for Earth Science, CAS, China

ARTICLE INFO

Keywords:
Pelitic granulites
Cordierite
Kyanite
High-pressure granulite-facies
Paleoproterozoic plate tectonics

ABSTRACT

The pelitic granulites along the Paleoproterozoic Jiao-Liao-Ji belt (JLJB) are dominated by cordierite/sillimanite-bearing low- to medium-pressure (LMP) conditions. Recent studies have recognized a few typical high-pressure (HP) pelitic granulites without retrograde cordierite from the Jiaobei terrane, the southern part of the JLJB. The relationship between the dominant LMP and rare HP pelitic granulites is not well constrained, and whether the LMP types are retrograde products of the HP ones remains uncertain. This uncertainty precludes a full understanding of the original spatial distribution of HP pelitic granulites and the tectonic affinity of the JLJB. We identify in this study for the first time, relict kyanite and the mineral assemblage of kyanite + K-feldspar + rutile + garnet from typically cordierite/sillimanite-bearing LMP pelitic granulites within the Jiaobei terrane. Integrated results from petrology, pseudosection modeling, geothermobarometry, and zircon and monazite U-Pb geochronology suggest that these LMP pelitic granulites experienced an earlier HP granulite-facies metamorphism possibly at ~1.95 Ga, with minimum *P-T* conditions of 13–14 kbar and 860–870 °C. Subsequently, these rocks underwent near isothermal decompression to 4–7 kbar and > 840 °C, followed by isobaric cooling to ~600 °C and 4–6 kbar. The decompression and cooling triggered LMP granulite-facies retrogression at ~1.85 Ga that eclipsed the earlier HP granulite-facies records. The clockwise *P-T-t* path defined is consistent with those reported from typical HP pelitic and mafic granulites elsewhere in the Jiaobei terrane. The results confirm that at least some portions of the typically cordierite/sillimanite-bearing LMP pelitic granulites are retrograded from the HP types. This greatly expands the spatial distribution of HP pelitic granulites and suggests a linear HP granulite-facies metamorphic belt within the Jiaobei terrane. The linear distribution of HP pelitic granulites whose protoliths are sedimentary rocks from Earth's surface and the consistent clockwise *P-T-t* paths require Paleoproterozoic subduction, collision, and exhumation processes similar to those operating in modern plate tectonics. Our results from the JLJB thus provide new metamorphic constraints on the nature of Paleoproterozoic plate tectonics, and have implications for other Precambrian high-grade terranes worldwide where pelitic granulites are dominated by LMP types.

1. Introduction

Recent studies have hypothesized that the horizontal movements of the lithosphere due to plate tectonics might have started in early Precambrian (e.g., Cawood et al., 2013; Holder et al., 2019; Sobolev and Brown, 2019; Xu et al., 2018a). However, insufficient early Precambrian geological records indicative of modern plate tectonics have kept alive the debate about when and in what form plate tectonics emerged on Earth (Chowdhury and Chakraborty, 2019; Holder et al., 2019). Early Precambrian high-grade terranes or tectonic belts are the only accessible records of geodynamic processes operated in the distant past (Brown and Johnson, 2018; Chowdhury and Chakraborty, 2019;

* Corresponding author at: State Key Laboratory of Lithospheric Evolution, Institute of Geology and Geophysics, Chinese Academy of Sciences, Beijing 100029, China.
E-mail address: mgzhai@mail.igcas.ac.cn (M. Zhai).

https://doi.org/10.1016/j.precamres.2020.105677
Received 11 September 2019; Received in revised form 10 January 2020; Accepted 24 February 2020
Available online 26 February 2020

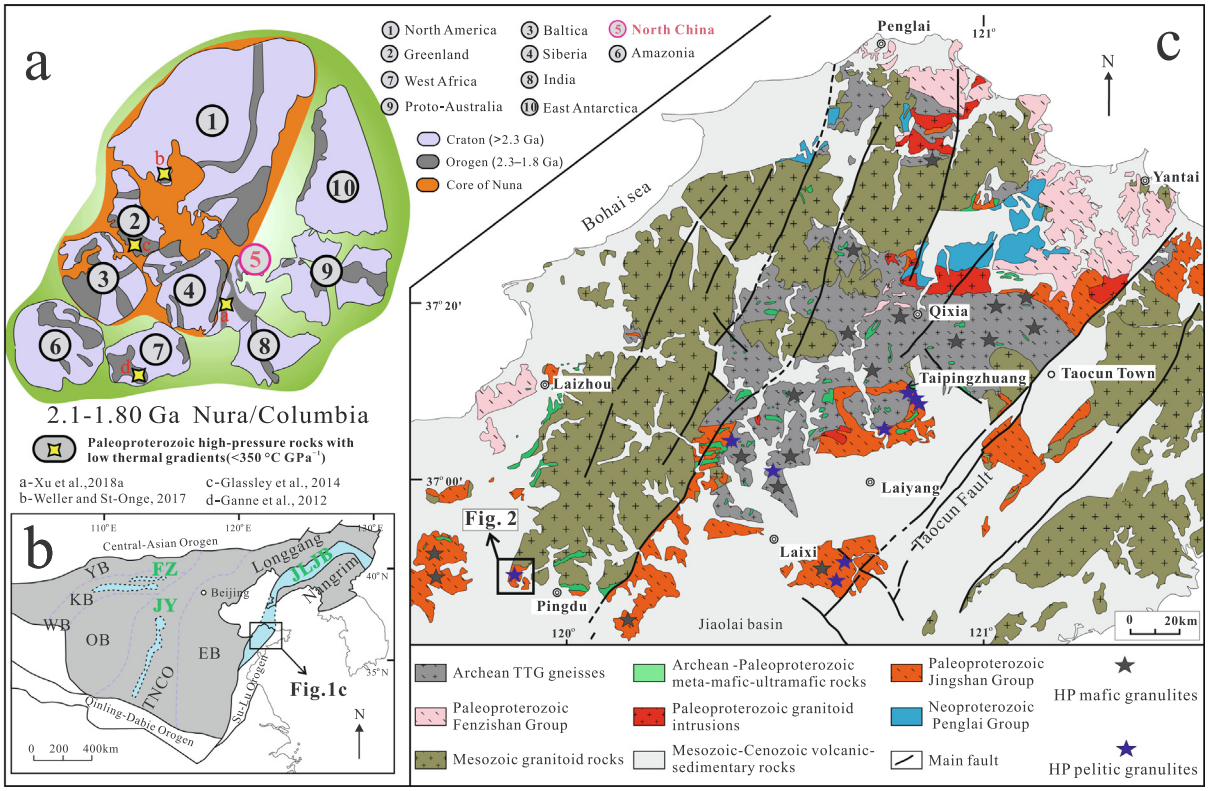

Fig. 1. (a) Constructed supercontinent Columbia/Nuna during 1.8–2.1 Ga (modified after Wan et al., 2015). The locations of Paleoproterozoic high-pressure rocks with low thermal gradient (< 10 °C/km) (Ganne et al., 2012; Glassley et al., 2014; Weller and St-Onge, 2017; Xu et al., 2018a) and positions of the North China Craton are marked. (b) Simplified geological map showing Paleoproterozoic tectonic division of the North China Craton and the location of the Jiaobei terrane (modified after Zhao and Zhai, 2013). EB, Eastern Block; FZ, Fenzhen belt; JLJB, Jiao-Liao-Ji belt; JY, Jinyu belt; KB, Khondalite belt; OB, Ordos Block; TNCO, Trans-North China Orogen; WB, Western Block; YB, Yinshan Block. (c) Regional geological map of the Jiaobei terrane (modified after Li et al., 2017; Zou et al., 2019).

Holder et al., 2019; Weller and St-Onge, 2017; Xu et al., 2018a; Zhai, 2009; Zhao et al., 2001; Zhou et al., 2017). Metamorphic products within these ancient high-grade terranes are mainly upper amphibolite- to granulite-facies rocks (Brown and Johnson, 2018; Harley, 1989; Lu and Jin, 1993; Lu et al., 1996; O'Brien and Rotzler, 2003; Zhai, 2009; Zhou et al., 2017), of which the high-pressure (HP) pelitic granulites are considered to reflect geodynamic processes similar to subduction and collision in modern plate tectonics (e.g., O'Brien and Rotzler, 2003; Tam et al., 2012c; Wu et al., 2016; Yin et al., 2015; Zhou et al., 2004, 2008b; Zou et al., 2019). In addition, a diagnostic feature of modern convergent plate margins is the linear distribution pattern on a regional scale of their metamorphic products (e.g., Liou et al., 2004). Hence, the linear distribution of HP pelitic granulites can serve as reliable criteria to identify the past operation of plate tectonics. Quantified metamorphic pressure–temperature-time (*P-T-t*) paths of these special rocks can therefore constrain the nature of Precambrian plate tectonics (Brown, 2014).

However, HP pelitic granulites that are defined by the key mineral assemblage of kyanite + garnet + ternary feldspar + rutile are rare or even potentially absent in many early Precambrian high-grade terranes worldwide (e.g., Brown, 2014; Harley, 1989; O'Brien and Rotzler, 2003; Wu et al., 2016; Yin et al., 2015; Zou et al., 2019). Pelitic granulites in these ancient terranes are pervasively dominated by cordierite/sillimanite-bearing low- to medium-pressure (LMP) types (e.g., Harley, 1989; Liu et al., 2019; Lu et al., 1996; Prakash, 1999; Turkina and Sukhorukov, 2015; Yan et al., 1991). Tectonic processes responsible for the formation of the LMP pelitic granulites are non-unique. The burial of sedimentary precursors of LMP pelitic granulites and subsequent near isothermal decompression (ITD) paths do not necessarily reflect crustal thickening, but can potentially occur within a deep rift-style basin (Francois et al., 2014; Tucker et al., 2015; Wickham and Oxburgh, 1985). Moreover, the rarity of HP pelitic granulites also raises the possibility that they may plausibly have formed via localized overpressure generated in crustal shear zones (e.g., Chu et al., 2017; Schmalholz and Podladchikov, 2013) at a shallower depth similar to that of LMP types. In many cases, the relationship between the rare HP pelitic granulites and the dominant LMP types remains elusive, and whether the dominant LMP rocks are retrograde products of the HP ones is a topic of further controversy. Such uncertainty poses a substantial challenge to the accurate tectonic interpretation of Precambrian high-grade metasedimentary rocks, and has been a hindrance to retrieving original spatial distributions of HP pelitic granulites and understanding the nature of lithospheric processes in early Earth.

The Paleoproterozoic Jiao-Liao-Ji belt (JLJB) provides an opportunity to study the relationship between the dominant LMP and rare HP pelitic granulites, and to constrain the prevailing style of Paleoproterozoic plate tectonics, at least in that part of the world. The JLJB hosts abundant meta-sedimentary and meta-volcanic successions typical of the khondalite series rocks (Liu et al., 2015a). The pelitic granulites along the JLJB are dominated by cordierite/sillimanite-bearing LMP types (Cai et al., 2017; Liu et al., 2015a; Lu et al., 1996; Tam et al., 2012a). Recent studies have identified a few localities for typical HP pelitic granulites without retrograde cordierite from the Jiaobei terrane, the southern part of the JLJB (Tam et al., 2012c; Wang et al., 2010; Zhou et al., 2004, 2008b; Zou et al., 2017, 2019). Although the exposures for typical HP pelitic granulites may continuously increase (Zou et al., 2019), whether the dominant cordierite/sillimanite-bearing LMP pelitic granulites are retrograded from HP pelitic granulites is still controversial. One of the main uncertainties in connecting the typical HP pelitic granulites and the dominant cordierite/sillimanite-bearing LMP rocks is that the direct observation of 'intermediate products' that are expected to be characterized by kyanite relics (HP

granulite-facies stage) and retrograde cordierite (LMP granulite-facies stage) is lacking.

We identify in this study for the first time, kyanite relics and the mineral assemblage of kyanite + K-feldspar + rutile + garnet from typically cordierite/sillimanite-bearing LMP pelitic granulites within the Jiaobei terrane, and present associated detailed petrology, quantitative *P-T* path calculation, and zircon and monazite U-Pb geochronology. Our results confirm that at least some portions of the typical LMP pelitic granulites are retrograded from the HP types during hot decompression and cooling at ~1.85 Ga. This restores the original linear distribution of HP pelitic granulites within the Jiaobei terrane and suggests Paleoproterozoic plate tectonics similar to modern times. The results thus have implications for other ancient high-grade terranes worldwide where pelitic granulites are dominated by LMP rocks, and shed more light on the nature of Paleoproterozoic plate tectonics involved in the formation of the JLJB.

2. Geological setting

The Paleoproterozoic history of the North China Craton is mainly recorded in three principal tectonic belts, termed the Fengzhen belt (Khondalite belt), the Jinyu mobile belt (Trans-North China Orogenic belt) and the Jiao-Liao-Ji belt (JLJB; Fig. 1b; Zhai and Liu, 2003; Zhao and Zhai, 2013). The tectonic evolution of these three Paleoproterozoic belts/orogens has been a major topic of interest, mainly regarding their roles in constraining the position of North China in reconstructions of supercontinent Columbia/Nuna (Fig. 1a; Evans and Mitchell, 2011; Kusky and Li, 2003; Trap et al., 2007; Zhai and Santosh, 2011; Zhao et al., 2002) and the tectonic regimes related to global establishment of modern plate tectonics featuring cold deep subduction (e.g., Weller and St-Onge, 2017; Xu et al., 2018a). Decoding tectonic processes involved in these tectonic belts can help to evaluate existing hypotheses concerning when plate tectonics emerged and how it evolved through time (Holder et al., 2019).

The Paleoproterozoic Jiao-Liao-Ji belt (JLJB) extends NE-SW for ~1200 km, separating the Longgang block from the Nangrim block (Fig. 1b; Liu et al., 2015a; Zhao and Zhai, 2013). The JLJB is mainly comprised of meta-sedimentary and meta-volcanic successions and a range of granitoid to mafic intrusions (Liu et al., 2015a; Xu and Liu, 2019). These successions include from northeast to southwest, the Macheonayeong Group in North Korea, the Laoling and Ji'an Groups in southern Jilin, the North and South Liaohe Groups in the Liaodong area, the Fenzishan and Jingshan Groups in the Jiaobei terrane, and the Wuhe Group in Anhui Province (Li and Zhao, 2007; Li et al., 2011, 2012; Liu et al., 2015c; Lu et al., 1996; Luo et al., 2004; Tam et al., 2011; Tian et al., 2017; Zou et al., 2018). These sedimentary successions were deposited during 2.2–2.1 Ga (e.g., Xu et al., 2018b) and were metamorphosed at 1.95–1.80 Ga (Liu et al., 2015a). Stratigraphic characteristics broadly shared by these successions feature (from bottom to top) a basal clastic-rich sequence and a lower bimodal-volcanic sequence, a middle carbonate-rich sequence, and an upper pelitic-rich sequence (Lu et al., 1996; Wang, 1995). Subsequent high-grade metamorphism and deformation disturbed the original sedimentary layering. Recent studies have traced clockwise metamorphic *P-T-t* paths with typical ITD trajectories from these successions (e.g., Cai et al., 2017; Liu et al., 2015c; Tam et al., 2012a, 2012c; Tian et al., 2017; Zhou et al., 2004; Zou et al., 2017), indicating that ancient tectonic processes operated in a similar manner to modern continental collision.

Our study area, the Jiaobei terrane, is located at the southwestern part of the JLJB (Fig. 1b–c). Its main units include the Archean basement rocks, Paleoproterozoic Fenzishan and Jingshan Groups, Meso-Neoproterozoic Zhifu and Penglai Groups (Fig. 1c), all of which are locally intruded by Mesozoic granitoids and covered by Cenozoic sediments. The Archean basement rocks are dominated by tonalitic-trondhjemitic-granodioritic (TTG) gneisses, with minor amounts of supracrustal rocks. Zircon U-Pb geochronology on Archean basement rocks reveals multi-stage magmatism at ~2.9 Ga, ~2.7 Ga and ~2.5 Ga, and two metamorphic events at ~2.5 Ga and 1.95–1.80 Ga (e.g., Jahn et al., 2008; Liu et al., 2011a, 2013a, 2015b; Tang et al., 2007; Wang et al., 2014; Wu et al., 2014; Zhou et al., 2008a). Marble, slate and quartzite are the main rock types in the Penglai and Zhifu Groups deposited during 0.8–1.1 Ga and > 1.80 Ga, respectively (Chu et al., 2011; Li et al., 2007; Liu et al., 2013b; Zhou et al., 2008a).

The Paleoproterozoic Jingshan and Fenzishan Groups are lithologically representative of the JLJB, and thus are ideal targets to decode its tectonic evolution. These two groups have similar protolith and ore-bearing characteristics (Wang, 1995), but differ in the grades of metamorphism and their spatial distributions. The greenschist- to lower amphibolite-facies Fenzishan Group is mainly exposed in the northern and western parts of the Jiaobei terrane; the Jingshan Group is located in the southern and eastern parts, and was metamorphosed to upper amphibolite- and granulite-facies (Fig. 1c; Li et al., 2012; Liu et al., 2015c; Tam et al., 2012a, 2012c; Zhou et al., 2004). The pelitic granulites in the Jingshan Group are dominated by cordierite/sillimanite-bearing LMP conditions (Lu et al., 1996; Tam et al., 2012a). Recent studies have identified kyanite-bearing pelitic granulites (HP types) without cordierite from a few localities of the Jingshan Group (Liu et al., 2015c; Tam et al., 2012c; Zhou et al., 2004; Zou et al., 2019). Whether the dominant LMP pelitic granulites are retrograde products of the HP types is still a topic of controversy. This dispute is largely due to the lack of evidence showing kyanite relics (HP granulite-facies stage) and retrograde cordierite formation (LMP granulite-facies stage) from the same pelitic granulites.

3. Field setting and petrographic description

The studied samples were collected from the Jingshan Group exposed in the Mingcun and Dongshiling villages, west of city Pingdu (Figs. 1c and 2). We distinguished three kinds of granulite-facies paragneisses according to their mineralogy, color, and texture in this region: (1) cordierite-bearing metapelites, (2) garnet-rich metapelites without cordierite and (3) graphite-bearing gneisses. The cordierite-bearing metapelites are the most abundant rocks (samples 17SD03, 17SD04, 17SD05 and 17SD07; Fig. 3a–b) that are characterized by the coarse-grained aluminosilicate minerals (Fig. 4a). They occur as grey-brown, medium- to coarse-grained, deformed layers that alternate with variably diffuse quartz-feldspar layers (leucosomes; Fig. 4a), suggesting an in-situ anatectic melting process. The quartz-feldspar layers also locally disrupt the foliation defined by oriented sillimanite and biotite (Fig. 4a). Local cordierite-rich veins cut the foliation (Fig. 4a). The garnet-rich metapelites without cordierite (sample 17SD06; Fig. 3a) are light grey, medium-grained, and relatively massive in structure, with limited leucosomes (Fig. 5a). The garnet-rich metapelites are closely associated with the cordierite-rich metapelites exposed in the same shallow quarry (Fig. 3a). The graphite-bearing gneisses are dark in color and commonly associated with graphite ore (samples 18SD26 and 18SD27; Figs. 2 and 3c). In this area, we also observed some garnet-bearing intermediate-mafic granulites that occur as lenses within or dikes intruding the metapelites (Fig. 3d). We chose the samples 17SD05, 17SD06 and 17SD07 as representatives for detailed study, because only very minor graphite occurs in their thin sections and thus the effect of CO_2 flux on mineral assemblages should be insignificant. Their petrographic characteristics are summarized below.

3.1. Cordierite-bearing metapelites

The cordierite-bearing metapelites (samples 17SD05 and 17SD07) share similar petrographic features, and are mainly comprised of garnet, sillimanite/kyanite, quartz, cordierite, biotite, plagioclase, and K-feldspar (Fig. 4b–c), with minor accessory minerals of ilmenite, rutile, zircon, and monazite. Garnet generally occurs as porphyroblasts and can be divided into three domains: (1) a garnet core that is rich in

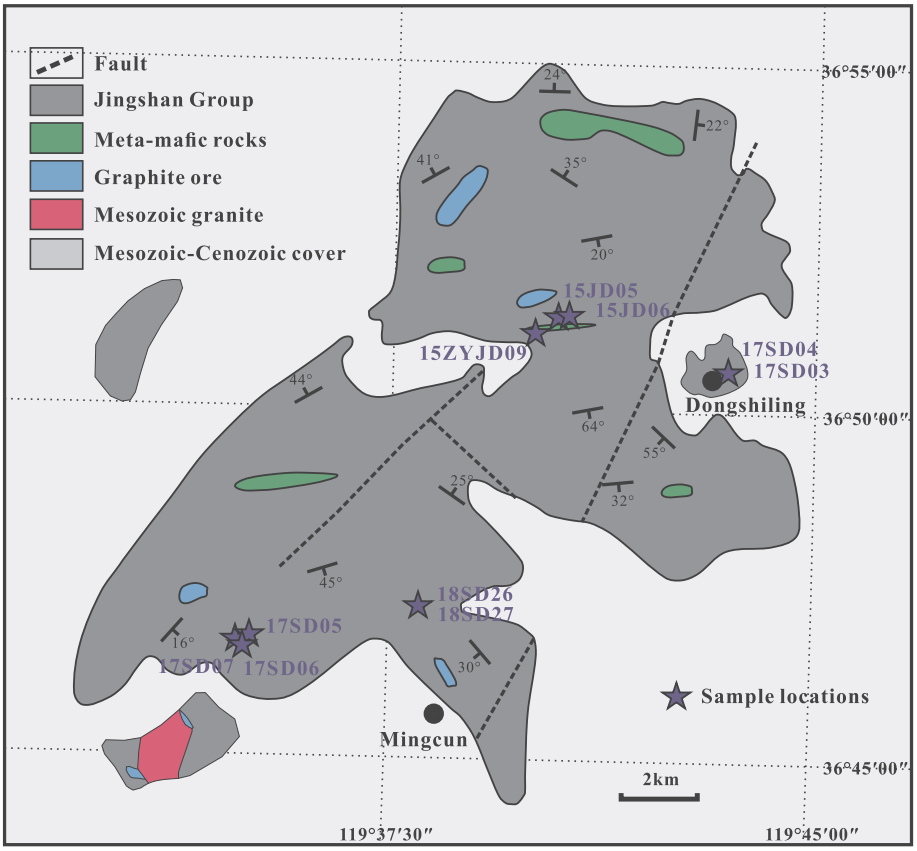

Fig. 2. Geological map showing the Jingshan Group and associated mafic granulites and graphite ores in the Mingcun-Dongshiling villages of the Jiaobei terrane. Blue stars represent sample locations. (For interpretation of the references to color in this figure legend, the reader is referred to the web version of this article.)

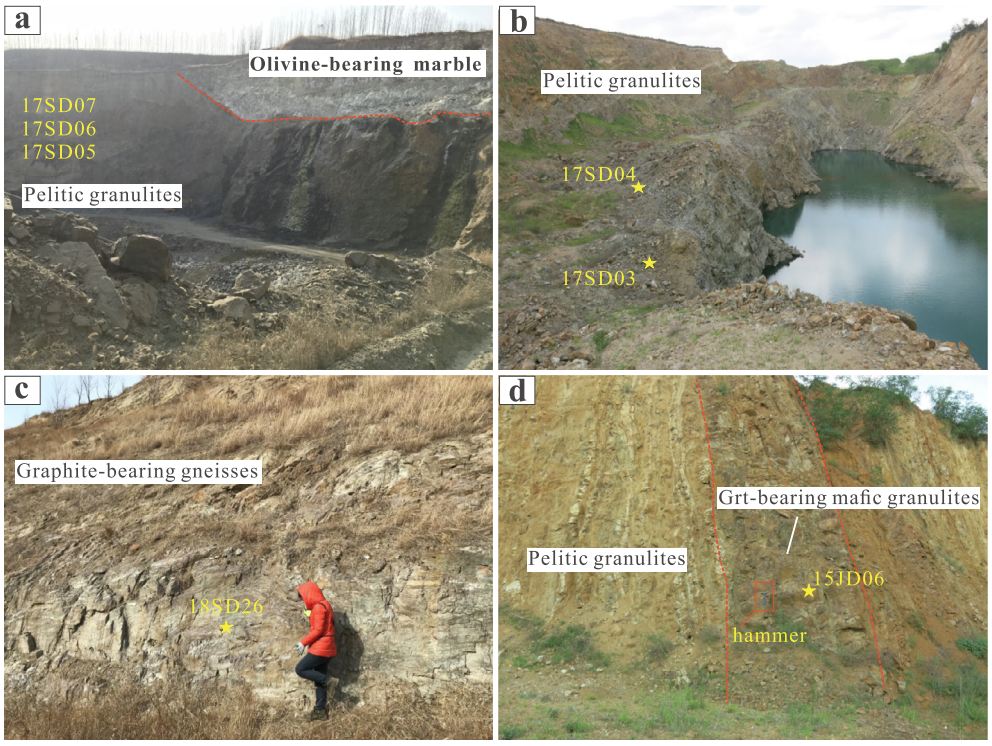

Fig. 3. Field photographs of the pelitic granulites in the Mingcun-Dongshiling villages. (a) Pelitic granulites 17SD05, 17SD06, 17SD07 and associated olivine-bearing marble in a shallow quarry. (b) Pelitic granulites 17SD03 and 17SD04 and (c) graphite-bearing gneisses. (d) Garnet-bearing mafic granulites occur as dikes intruding the pelitic granulites.

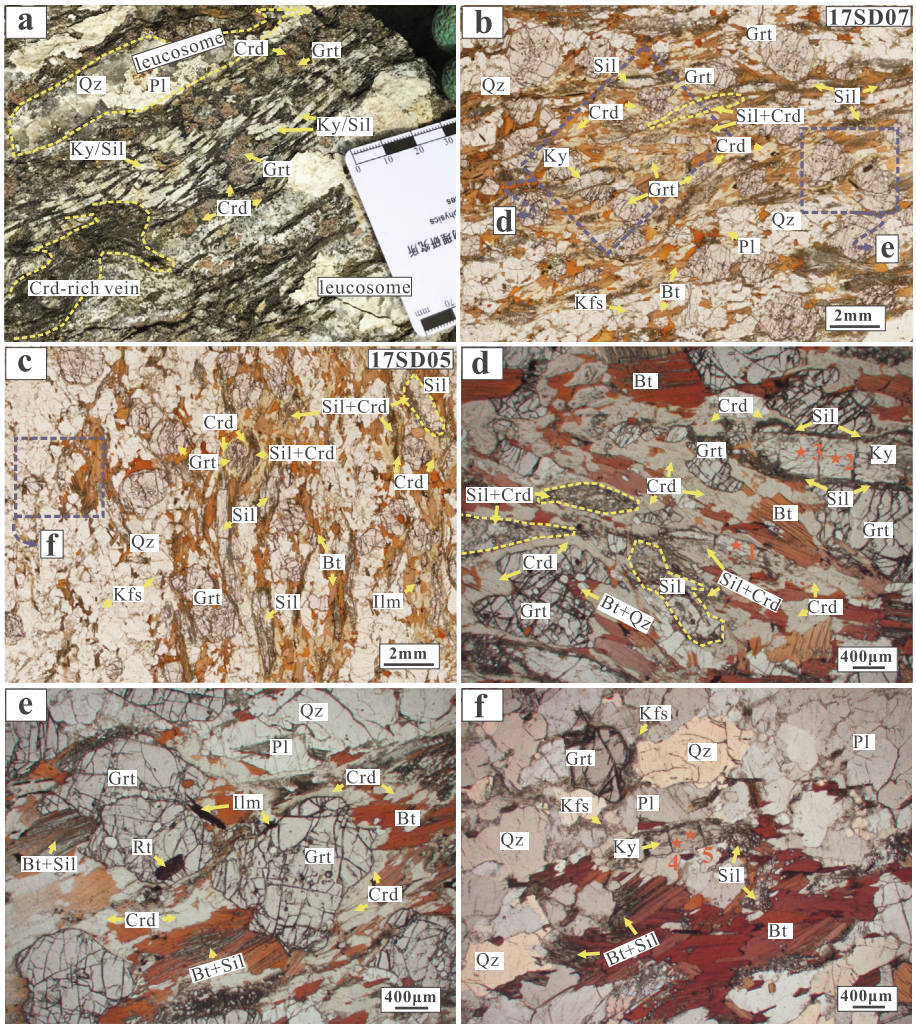

Fig. 4. Hand specimens and petrographic photographs of samples 17SD05 and 17SD07. (a) Large tabular kyanite/sillimanite and corroded garnet grains moated by cordierite. Note the quartz-feldspar layers that run parallel to but also locally disrupt the foliation defined by oriented sillimanites. Local cordierite-rich veins crosscut the foliation. (b) A part of thin section scanning image of sample 17SD07 charactering large tabular aluminosilicate minerals and intergrowths of cordierite + sillimanite. In cordierite-rich domains, garnet edges are variably absorbed by cordierite. In quartz-feldspar-rich domains, garnets have relatively well-preserved rims. Blue dash rectangles represent microdomains shown in Fig. 4d–e. (c) A part of thin section scanning image of sample 17SD05. Garnet grains within cordierite-rich domains show corroded margins by cordierite corona. Large matrix sillimanites have embayed rims by cordierite + sillimanite symplectites. The blue dash rectangle marks the position of microdomain shown in Fig. 4f. (d) A kyanite pseudomorph is rimmed by needle-like sillimanite aggregates. Some sillimanite + cordierite symplectites possess prismatic to tabular shapes and locally erode sillimanite porphyroblasts along margin. Note the cordierite corona around garnet, and local biotite + quartz ± sillimanite symplectites grow inside the garnet's rim. (e) A rutile inclusion within garnet and an ilmenite in the matrix. Biotite + sillimanite intergrowths develop inside garnet rim. (f) A kyanite pseudomorph in the quartz-feldspar-rich domain. Development of biotite + sillimanite intergrowths along margins of coarse-grained biotite aggregates. Red stars and numbers denote the locations and spots of Raman analyses shown in Fig. 6: Spots 1–5. (For interpretation of the references to color in this figure legend, the reader is referred to the web version of this article.)

mineral inclusions of quartz + rutile + biotite ± plagioclase ± K-feldspar (Figs. 4e, 7a–d and i–l), (2) a garnet mantle of rare inclusions (Fig. 7a–d and i–l), and (3) an inclusion-free garnet rim that is moated by cordierite corona or locally invaded by biotite + sillimanite symplectites (Fig. 4b–e). In cordierite-rich domains, garnet porphyroblasts are embayed by cordierite corona (Fig. 4b–d). Some sillimanite grains occur as porphyroblasts and are eroded by cordierite + sillimanite symplectites along their margins (Fig. 4b–e). A few sillimanite + cordierite symplectites have prismatic to tabular pseudomorphs of sillimanite (Fig. 4d). Notably, kyanite pseudomorphs are recognized (Fig. 4d and f), and in some instances are rimmed by fine-grained needle-like sillimanite aggregates (Fig. 4d). The Raman spectra reveal some weak peaks of kyanite from these pseudomorphs (~300, ~328, ~390, 487 and ~900 cm^{-1}; Fig. 6: Spots 2–5), and these peaks tend to shift towards the major peaks of sillimanite, confirming existence of kyanite relics. K-feldspar (perthite) and plagioclase are scattered in the matrix and are observed to be in contact with the kyanite pseudomorph (Fig. 4f). Metal oxides in matrix are dominated by ilmenite with very rare rutile. Rutile is preserved within garnet (Fig. 4e). Texturally late biotite + sillimanite ± plagioclase ± quartz symplectites or intergrowths grow inside garnet rims (Fig. 4e), and the sericite locally alters cordierite grains.

On the basis of the above reaction textures and mineral chemistry below, four metamorphic stages (M_1-M_4) can be defined. The prograde M_1 assemblage is comprised of minerals enclosed within garnet core (biotite + quartz + rutile ± plagioclase ± K-feldspar) plus the garnet core. During the prograde metamorphism, it is inferred that the following biotite dehydration reaction facilitates the growth of garnet and K-feldspar (e.g., Spear et al., 1999):

Biotite + quartz → garnet + K - feldspar + melt (R1)

For typical metapelites, K-feldspar and aluminosilicates are thought to form by muscovite dehydration melting reaction under lower *P-T* conditions (e.g., Spear et al., 1999; Yin et al., 2015):

Muscovite + quartz → aluminosilicates + K - feldspar + liquid/melt (R2)

The peak M_2 mineral assemblage equilibrated in kyanite-stability field, which is supported by kyanite pseudomorphs (Fig. 4d and f) and kyanite relics evident in Raman spectra (Fig. 6). Thus, the M_2 stage is interpreted to be represented by garnet (core to mantle domains) + kyanite + quartz + K-feldspar + plagioclase + rutile + ilmenite + melt phase ± biotite, suggestive of high-pressure granulite-facies (O'Brien and Rotzler, 2003).

The post-peak M_3 stage is characterized by the transformation of kyanite to sillimanite, rutile to ilmenite, and formation of cordierite in the matrix. Rutile is preserved within garnet and is rare in the matrix whose metal oxides are dominated by ilmenite. The sillimanite porphyroblasts of kyanite pseudomorphs are interpreted to directly transform from kyanite (Fig. 4d and f). Some sillimanite porphyroblasts are eroded by sillimanite + cordierite symplectites along margins and garnet is typically moated by cordierite (Fig. 4b–d). These petrographic characteristics suggest the following possible reactions (Bohlen and Liotta, 1986; Spear et al., 1999; Yin et al., 2015):

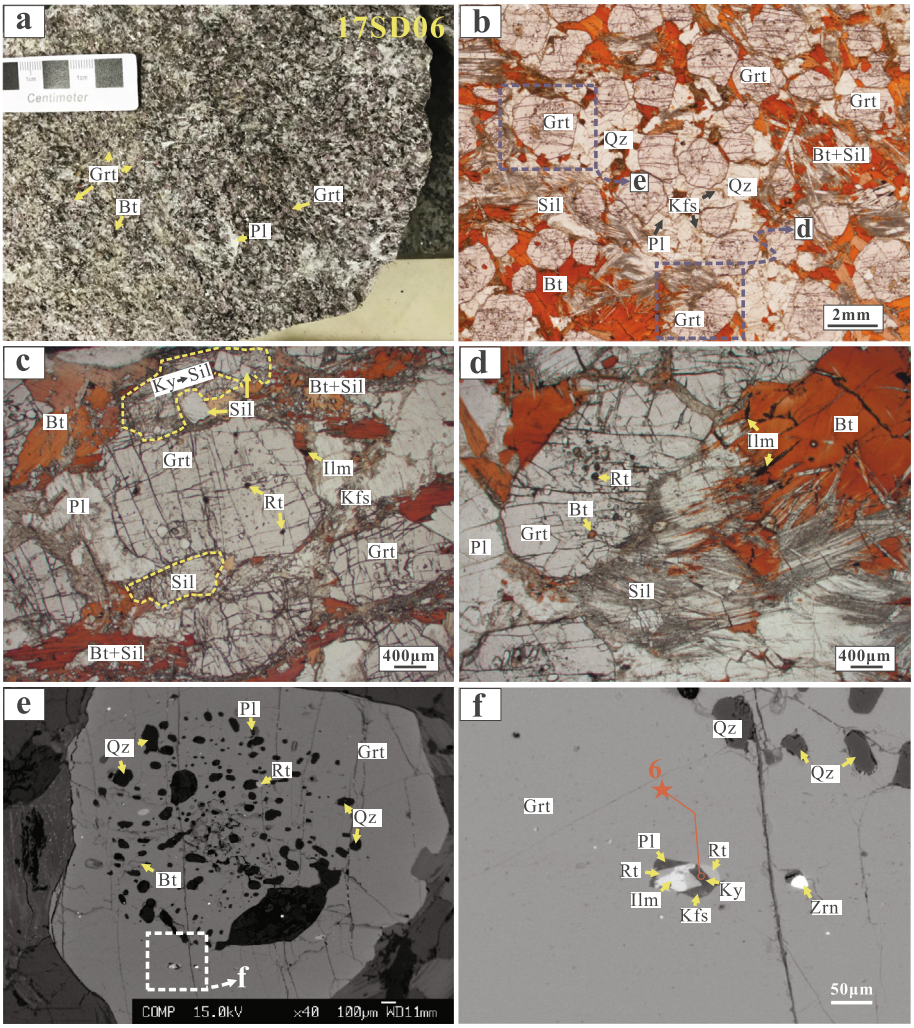

Fig. 5. Hand specimen and petrographic photographs of sample 17SD06. (a) A homogenous and massive structure in a hand specimen scale. (b) A part of thin section scanning image showing garnet porphyroblast in the matrix of plagioclase, biotite, K-feldspar, sillimanite and quartz, without cordierite. The matrix minerals lack obvious orientation. Blue dash rectangles mark the positions of microdomains shown in Fig. 5d–e. (c–d) Rutile grains are preserved within garnet. Metal oxides are dominated by ilmenite which also occurs as exsolution from biotite. Large tabular sillimanites have kyanite pseudomorph and some grains are invaded by a second generation of sillimanite. Local hair-like sillimanites develop along margins of biotite aggregates and grow inside garnet rims. (e) The garnet core contains inclusions of quartz, rutile, plagioclase, and biotite while the rim is inclusion-free. The white dash rectangle represents microdomain shown in Fig. 5f. (f) Polymineralic inclusions of rutile, kyanite, K-feldspar, plagioclase and ilmenite enclosed within garnet mantle. The red star and number denote the location and spot of Raman analysis shown in Fig. 6: Spot 6. (For interpretation of the references to color in this figure legend, the reader is referred to the web version of this article.)

Kyanite → sillimanite (R3)

Rutile + grossular + almandine → plagioclase + ilmenite + quartz (R4)

Sillimanite + garnet + melt → cordierite (R5)

Two types of cordierite occur in the matrix: the cordierite corona around garnet and the cordierite + sillimanite symplectites. Their difference can be explained by variation in local effective bulk rock compositions seen by the reaction R(5). These cordierites are in contact with K-feldspar and plagioclase in the matrix. It is noted that in the microdomains where cordierite is developed, biotite is relic or absent (Fig. 4d). In this case, we suggest that the M_3 assemblages developed at high temperature conditions where biotite is unstable. Therefore, the M_3 mineral assemblage is represented by garnet (rim domains) + sillimanite + cordierite + ilmenite + K-feldspar + plagioclase + quartz + melt.

The retrograde M_4 assemblage is indicated by the local development of texturally late biotite + sillimanite ± plagioclase ± quartz symplectites near garnet rims (Fig. 4e), pointing to melt-residue back reactions (Indares et al., 2008; Kriegsman and Alvarez-Valero, 2010; Spear et al., 1999; Waters, 2001; Zou et al., 2017), likely associated with final melt crystallization. Locally, this mineral assemblage shows a lineation parallel to that defined by other matrix minerals (Fig. 4e). The minor fine-grained sericite does not show a preferred orientation, indicating a very late alteration episode.

3.2. Garnet-rich metapelites

The distinguishing features of sample 17SD06 are the absence of cordierite and high volume proportions of garnet (up to 40–60 vol%; Fig. 5a–b). It contains 1–3 mm garnet porphyroblasts and matrix minerals consisting of moderately foliated biotite, sillimanite and granoblastic plagioclase, K-feldspar (perthite), and quartz (Fig. 5b). Garnet porphyroblasts commonly host abundant inclusions of quartz, biotite, and rutile, as well as minor plagioclase in the core (Fig. 5e); whereas the mantle is inclusion-sparse and the rim is inclusion-free (Fig. 5b–e). It is worth noting that polymineralic inclusions of rutile, kyanite, plagioclase, K-feldspar, and ilmenite are identified in garnet mantle domains (Fig. 5e–f; Fig. 6: Spot 6), suggestive of high-pressure granulite-facies metamorphism. Garnet porphyroblasts show embayed margins in contact with biotite + sillimanite symplectites (Fig. 5b–d), in comparison to the well-preserved edges close to quartz or feldspars (Fig. 5b–d). There are two kinds of sillimanite in the matrix: one is coarse-grained sillimanite (kyanite pseudomorph); the other is fibrous and associated with biotite, forming symplectites of biotite + sillimanite ± plagioclase ± quartz or occurring as aggregates near biotite (Fig. 5b–d). The polymineralic inclusions within the garnet mantle imply that the sample had been stable at high-pressure granulite-facies conditions and hence at least some coarse-grained sillimanites (kyanite pseudomorphs) in the matrix were once kyanite (Fig. 5c). Rutile is relatively well preserved within garnet (Fig. 5c–f), but is absent in the matrix. Metal oxide in the matrix is ilmenite, which also occurs as exsolutions within matrix biotite (Fig. 5d).

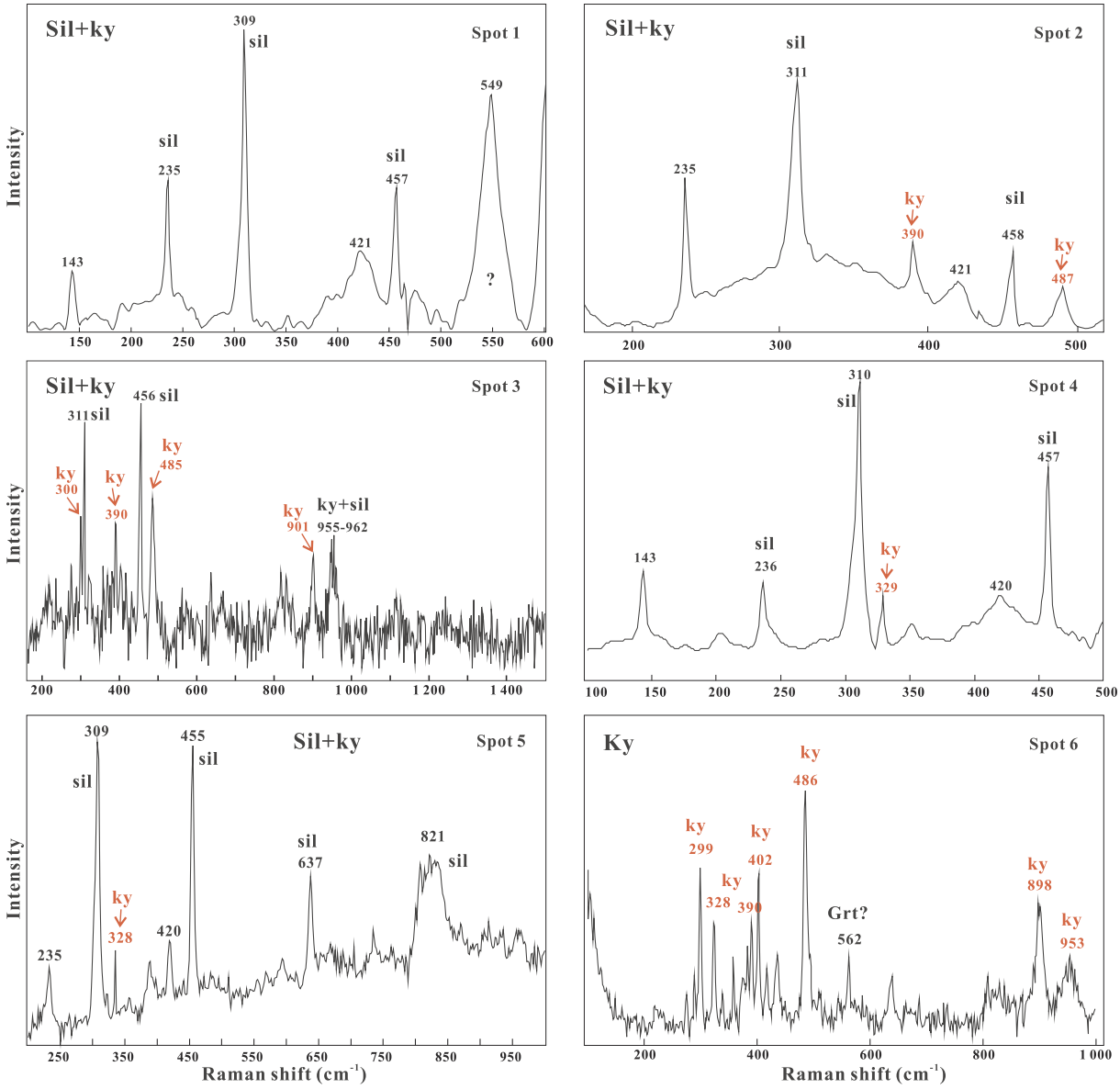

Fig. 6. Raman spectrum results with locations and spot numbers shown in Figs. 4d, f, and 5f. Note a bit of characteristic peaks of kyanite shown in Spots 2–5, and Spot 6 identifies an intact kyanite grain without any sillimanite peaks from polymineralic inclusions shown in Fig. 5f.

On the grounds of the above microtextures, we suggest an earlier prograde mineral assemblage (M_1) represented by mineral inclusions within garnet core (biotite + quartz + rutile + plagioclase ± K-feldspar) plus garnet core domains. The peak M_2 stage is interpreted to be stable at high-pressure granulite-facies conditions, featured by the mineral assemblage of kyanite + rutile ± ilmenite + garnet (mantle domains) + K-feldspar + plagioclase ± biotite + melt. This is overprinted by the M_3 assemblage of sillimanite + ilmenite + garnet (rim domains) + K-feldspar + plagioclase + melt ± biotite and a subsequent M_4 assemblage represented by biotite + sillimanite ± plagioclase ± quartz symplectites. The M_4 assemblage is related to a series of melt-residue back reactions, likely associated with melt crystallization (Indares et al., 2008; Kriegsman and Alvarez-Valero, 2010; Spear et al., 1999; Waters, 2001; Zou et al., 2017).

4. Analytical methods

In this contribution, we conducted Laser Raman Spectroscopy, mineral and whole rock chemistry, rutile and garnet geochemistry, and zircon and monazite U-Pb geochronology for the studied pelitic granulites.

4.1. Laser Raman spectroscopy, mineral and rock chemistry

The Laser Raman Spectroscopy was performed at the Institute of Geology and Geophysics, Chinese Academy of Sciences (IGGCAS) using the Lab Ram HR manufactured by HORIBA JOBIN YVON, France. Laser wavelength is 532 nm with a pulse frequency of 5 kHz. The scanning wave range was set to 100–1500 cm^{-1}. Spatial resolution is better than 1–2 μm. The representative results are shown in Fig. 6.

Mineral chemistry was analyzed using JEOL JXA-8100 electron microprobe (EMP) at the IGGCAS. Operating conditions were set to 15 kV accelerating voltage, 10nA beam current, 10–20 s counting time, and 1–5 μm spot sizes. Synthetic and natural minerals were used as standards. A further off-line correction was performed for iron-rich minerals such as garnet. Representative mineral compositions are listed in Tables 1–4.

Whole rock compositions of studied pelitic granulites were determined by X-ray fluorescence spectrometry (XRF, Axios MAX) at the Wuhan Sample Solution Analytical Technology Co. Ltd. The rock

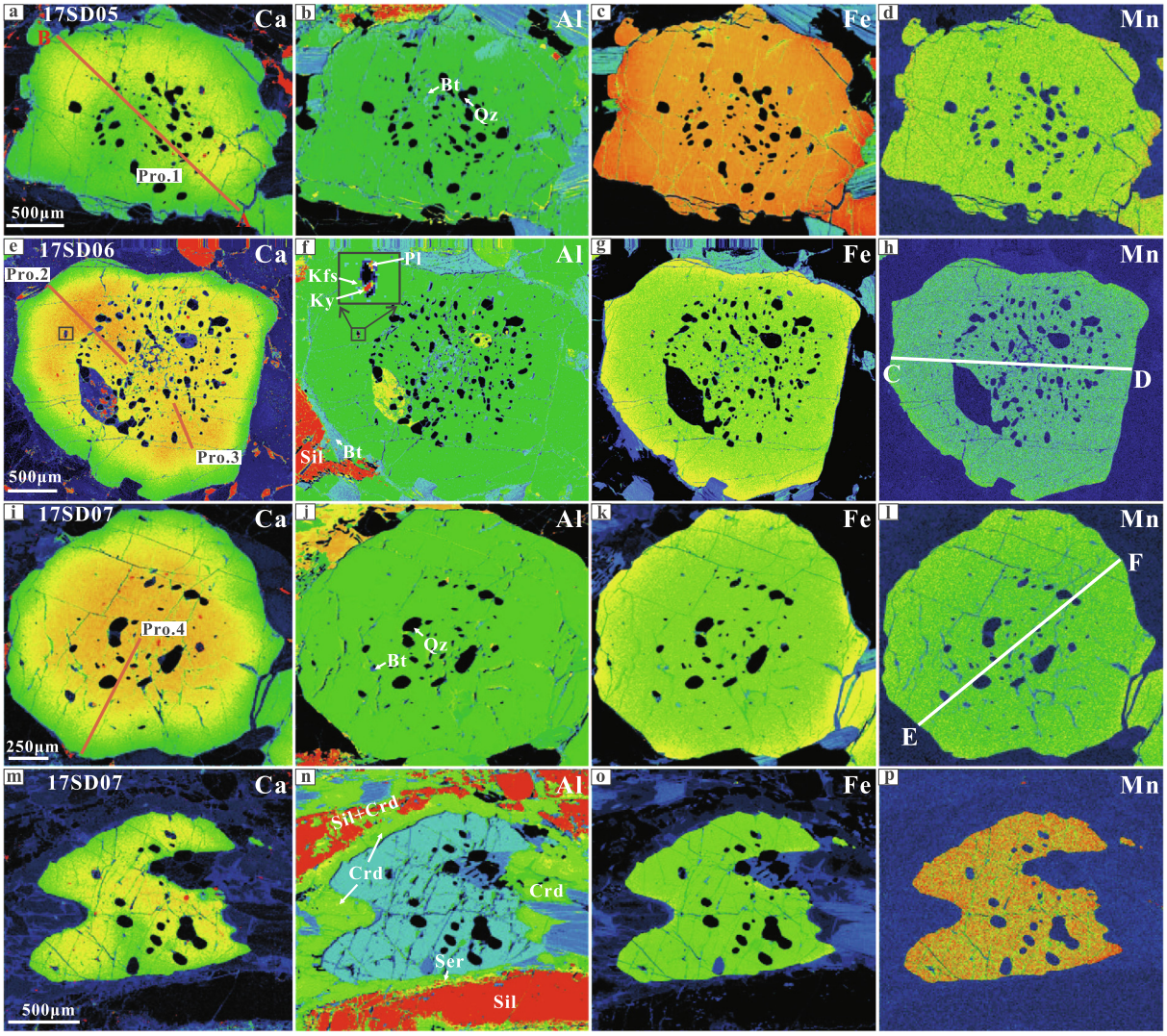

Fig. 7. Compositional maps for the selected garnets. The thick red lines represent the EMP profiles 1–4 shown in Fig. 8. The thick white lines (C–D and E–F) mark the traverses of REE analysis displayed in Fig. 14a–b. Note the polymineralic inclusions of kfs + ky + pl within the garnet mantle shown in Fig. 5f and 7f. In each map, warmer or brighter colors show higher concentrations. (For interpretation of the references to color in this figure legend, the reader is referred to the web version of this article.)

standards used the GSP-2, GBW07103 and GBW07316, which suggest precision and accuracy better than 5%. The FeO content was analyzed by chemical titration at the IGGCAS. The obtained whole rock compositions in mol% are presented in Table 5.

4.2. Rutile and garnet geochemistry

Determination of rutile (inclusions within garnet) geochemistry was performed using electron microprobe CAMECA SXFiveFE at the IGGCAS. The analytical method proposed by Zack et al. (2004) was adopted. The peak-background position was optimized and the operating conditions of 20 kV accelerating voltage, 100 nA beam current, 5 μm spot size and a total 14–15 min counting time were used. Detailed procedures are provided by Jiao et al. (2011). The detection limits for trace elements including Zr, Nb, Cr, Fe, Ta and Si are less than ~100 ppm. Data with high Si contents and unusual higher Zr contents than other rutile grains were excluded for temperature calculation. We also excluded high Nb (> 17000 ppm) data according to the suggestion by Zack et al. (2004). The Zr-in-rutile thermometry of Tomkins et al. (2007) was applied in this study, and the pressure input was defined by phase modeling and conventional barometer. The rutile geochemistry and calculated temperature results are given in Supplementary Table S1.

Measurement of garnet trace element concentrations was conducted using Agilent 7500a Q-ICP-MS equipped with 193 nm laser ablation system at the IGGCAS. The analytical procedures followed those described by Xie et al. (2008). Analytical conditions were 25 J/cm^2 laser energy density, 10 Hz laser repetition, and ~40 μm spot sizes. NIST 610 and 612 glasses were used as standards and Si as an internal standard element. The software GLITTER 4.0 (Macquarie University) was used for data reduction. The garnet trace element compositions obtained are listed in Supplementary Table S2.

4.3. Monazite and zircon U-Pb geochronology

Monazite and zircon crystals from samples 17SD06 and 17SD07 were extracted from crushed samples using heavy liquid and magnetic separation techniques at Wuhan Sample Solution Analytical Technology Co. Ltd. The extracted grains were further handpicked by binocular microscope. The collected zircon and monazite grains were mounted in epoxy resins. Characterization of zircon and monazite internal structures was made by performing cathodoluminescence (CL) and backscattered electron (BSE) images, as well as reflected light and transmitted micrographs.

Table 1
Representative composition of garnet from samples 17SD05, 17SD06 and 17SD07.

Sample	17SD07							
Texture	Core	Core	Mantle	Mantle	Mantle	Mantle	Rim	Rim
SiO_2	38.80	38.64	38.95	38.05	38.02	39.49	38.76	38.93
TiO_2	0.04	0.02	0.02	0.02	0.03	0.06	0.01	0.02
Al_2O_3	21.37	21.53	21.66	23.32	23.02	22.55	21.69	22.88
Cr_2O_3	0.01	0.02	0.02	0.12	0.15	0.03	0.02	0.01
FeO^T	29.81	29.62	29.56	29.39	29.02	29.72	31.34	32.39
MnO	0.45	0.42	0.48	0.42	0.46	0.47	0.50	0.54
MgO	7.44	7.68	7.59	8.41	8.35	7.51	6.97	6.13
CaO	2.47	2.19	2.20	2.10	2.12	1.90	1.48	1.13
Total	100.38	100.10	100.46	101.82	101.17	101.72	100.78	102.03
O	12	12	12	12	12	12	12	12
Si	3.012	3.003	3.016	2.889	2.906	3.020	3.012	3.000
Ti	0.002	0.001	0.001	0.001	0.002	0.003	0.001	0.001
Al	1.955	1.971	1.977	2.087	2.074	2.032	1.987	2.078
Cr	0.001	0.001	0.001	0.007	0.009	0.002	0.001	0.001
Fe^{3+}	0.016	0.019	0.000	0.125	0.102	0.000	0.000	0.000
Fe^{2+}	1.919	1.905	1.914	1.741	1.753	1.901	2.036	2.087
Mn	0.029	0.027	0.031	0.027	0.030	0.030	0.033	0.036
Mg	0.861	0.889	0.876	0.952	0.952	0.856	0.808	0.704
Ca	0.205	0.182	0.182	0.171	0.174	0.156	0.123	0.094
Total	8.000	8.000	8.000	8.000	8.000	8.000	8.000	8.000
X_{Mg}	0.31	0.32	0.31	0.35	0.35	0.31	0.28	0.25
Prp	0.286	0.296	0.290	0.329	0.327	0.283	0.268	0.235
Alm	0.637	0.634	0.638	0.602	0.603	0.653	0.680	0.721
Grs	0.067	0.060	0.061	0.055	0.057	0.054	0.041	0.032
Sps	0.010	0.009	0.010	0.009	0.010	0.010	0.011	0.012

Sample	17SD06						17SD05					
Texture	Core	Core	Mantle	Mantle	Rim	Rim	Rim	Mantle	Mantle	Core	Core	Rim
SiO_2	38.06	39.28	39.15	40.65	39.30	38.83	39.35	39.39	39.54	39.29	38.50	38.60
TiO_2	0.01	0.04	0.01	0.00	0.03	0.03	0.03	0.08	0.00	0.02	0.07	0.03
Al_2O_3	19.38	20.09	20.84	19.35	19.25	19.29	19.58	20.08	20.11	20.16	19.71	20.08
Cr_2O_3	0.80	0.04	0.02	0.12	0.00	0.02	0.00	0.00	0.03	0.02	0.00	0.04
FeO^T	29.60	29.10	29.50	27.99	30.25	31.50	32.34	30.46	30.47	30.59	30.40	31.64
MnO	0.42	0.37	0.39	0.38	0.42	0.46	0.51	0.41	0.50	0.38	0.42	0.52
MgO	8.00	8.55	8.46	8.10	7.93	7.39	6.67	7.41	7.47	7.69	7.59	7.06
CaO	2.03	2.00	2.14	2.04	1.45	1.32	1.52	2.29	1.99	1.82	1.61	1.26
Total	98.29	99.47	100.50	98.64	98.63	98.85	100.01	100.12	100.10	99.96	98.29	99.23
O	12	12	12	12	12	12	12	12	12	12	12	12
Si	3.023	3.064	3.023	3.203	3.112	3.082	3.101	3.076	3.088	3.070	3.062	3.055
Ti	0.000	0.003	0.000	0.000	0.002	0.002	0.002	0.004	0.000	0.001	0.004	0.002
Al	1.814	1.847	1.896	1.797	1.797	1.805	1.819	1.848	1.852	1.856	1.847	1.873
Cr	0.050	0.002	0.001	0.007	0.000	0.001	0.000	0.000	0.002	0.001	0.000	0.003
Fe^{3+}	0.090	0.017	0.057	0.000	0.000	0.025	0.000	0.000	0.000	0.001	0.022	0.011
Fe^{2+}	1.876	1.881	1.848	1.844	2.003	2.066	2.131	1.989	1.990	1.997	2.000	2.083
Mn	0.028	0.025	0.025	0.026	0.028	0.031	0.034	0.027	0.033	0.025	0.028	0.035
Mg	0.947	0.994	0.973	0.951	0.935	0.875	0.784	0.863	0.869	0.895	0.900	0.833
Ca	0.172	0.167	0.177	0.173	0.123	0.112	0.129	0.192	0.166	0.152	0.137	0.107
Total	8.000	8.000	8.000	8.000	8.000	8.000	8.000	8.000	8.000	8.000	8.000	8.000
X_{Mg}	0.34	0.35	0.34	0.34	0.32	0.30	0.27	0.30	0.30	0.31	0.31	0.29
Prp	0.313	0.324	0.322	0.297	0.300	0.284	0.253	0.280	0.281	0.292	0.294	0.272
Alm	0.621	0.613	0.611	0.634	0.650	0.670	0.694	0.648	0.653	0.650	0.652	0.681
Grs	0.053	0.054	0.057	0.061	0.040	0.036	0.042	0.063	0.055	0.050	0.044	0.035
Sps	0.009	0.008	0.008	0.009	0.009	0.010	0.011	0.009	0.011	0.008	0.009	0.011

Note: FeO^T is total FeO, and Fe^{3+} is estimated by stoichiometric calculation of Droop (1987).

Monazite U-Th-Pb isotopes were determined by CAMECA IMS-1280 ion microprobe (SIMS) at the IGGCAS. Detailed descriptions of analytical method and conditions refer to Li et al. (2013). The primary O^{2-} ion beam was accelerated at 13 kV with an intensity of ca. 2–3 nA, and the analytical spot size at sample surface was around 20 × 30 μm. Standard monazite RW-1 (Ling et al., 2017) was used as internal standard and monazite 44069 (Aleinikoff et al., 2006) as external standard. Calibration of U-Th-Pb isotopic ratios of unknowns was based on protocols of Li et al. (2013). Common Pb correction was conducted by applying the ^{207}Pb-^{230}Th based method (Williams, 1998; Li et al., 2013). All the monazite U-Th-Pb data are given in Supplementary Data Table S3.

Simultaneous measurement of zircon U-Th-Pb isotopes and rare earth elements (REE) was conducted using an Agilent 7500a Q-ICP-MS equipped with a 193-nm laser ablation system hosted at the IGGCAS. The analytical protocols of Xie et al. (2008) were adopted. We used analytical conditions of 30 J/cm^2 laser energy density, 15 Hz laser repetition and ~32 μm spot sizes. The zircons 91500 (Wiedenbeck et al., 2004) and Plesovice (Slama et al., 2008) were respectively employed as external and internal standards. NIST 610 glass was used as external standard and Si as an internal standard element to calibrate zircon REE concentrations. Data reduction was conducted using the GLITTER 4.0 program (Macquarie University). The zircon U-Th-Pb isotopic data are given in Supplementary Table S4 while the REE data are listed in Supplementary Table S5. All the U-Pb isotopic data were processed using Isoplot 3. 75 program (Ludwig, 2012). Uncertainty of individual

Table 2
Representative compositions of plagioclase and K-feldspar from samples 17SD05, 17SD06 and 17SD07.

Sample	17SD05						
Texture	Inclusion	Inclusion	Core	Core	Rim	Fine	kfs
SiO_2	58.21	58.81	58.66	58.01	58.20	59.18	64.19
TiO_2	0.05	0.08	0.03	0.04	0.01	0.02	0.04
Al_2O_3	24.12	24.00	25.01	24.81	25.44	25.59	18.65
Cr_2O_3	0.06	0.09	0.01	0.02	0.00	0.01	0.00
FeO^T	0.34	0.44	0.04	0.23	0.02	0.09	0.48
MnO	0.00	0.00	0.00	0.00	0.00	0.03	0.02
MgO	0.13	0.14	0.03	0.07	0.02	0.01	0.04
CaO	6.32	6.05	6.51	7.11	8.46	7.61	0.04
Na_2O	8.91	8.96	8.26	7.20	6.71	6.97	0.29
K_2O	0.36	0.36	0.11	0.19	0.12	0.09	15.59
Total	98.54	98.98	98.65	97.68	98.96	99.62	99.37
O	8.000	8.000	8.000	8.000	8.000	8.000	8.000
Si	2.656	2.669	2.655	2.652	2.629	2.649	2.982
Ti	0.002	0.003	0.001	0.001	0.000	0.001	0.002
Al	1.297	1.284	1.335	1.337	1.355	1.350	1.021
Cr	0.002	0.003	0.000	0.001	0.000	0.000	0.000
Fe	0.013	0.017	0.002	0.009	0.001	0.003	0.019
Mn	0.000	0.000	0.000	0.000	0.000	0.001	0.001
Mg	0.009	0.009	0.002	0.005	0.001	0.001	0.003
Ca	0.309	0.294	0.316	0.348	0.409	0.365	0.002
Na	0.788	0.788	0.725	0.638	0.588	0.605	0.026
K	0.021	0.021	0.006	0.011	0.007	0.005	0.924
An	0.28	0.27	0.30	0.35	0.41	0.37	0.00
Ab	0.70	0.71	0.69	0.64	0.59	0.62	0.03
Or	0.02	0.02	0.01	0.01	0.01	0.01	0.97

Sample	16SD06								17SD07							
Texture	Inclusion	Inclusion	Core	Core	Rim	Rim	Fine	kfs	Inclusion	Inclusion	Core	Core	Rim	Rim	Fine	kfs
SiO_2	60.00	58.74	58.56	59.68	57.96	55.87	55.13	64.81	58.68	59.23	58.40	57.88	57.93	57.73	57.84	64.82
TiO_2	0.02	0.08	0.03	0.03	0.04	0.00	0.00	0.02	0.01	0.02	0.04	0.02	0.03	0.03	0.01	0.04
Al_2O_3	24.08	23.97	24.08	26.03	24.52	27.23	27.41	17.91	24.09	24.12	24.66	25.36	25.55	24.15	24.42	18.21
FeO^T	0.03	0.27	0.14	0.01	0.23	0.48	0.11	0.03	0.22	0.20	0.11	0.08	0.00	0.00	0.09	0.00
MnO	0.01	0.00	0.01	0.03	0.00	0.00	0.01	0.01	0.00	0.00	0.00	0.03	0.00	0.00	0.00	0.00
MgO	0.02	0.18	0.04	0.01	0.04	0.07	0.00	0.01	0.02	0.03	0.01	0.00	0.01	0.01	0.01	0.01
CaO	6.61	5.31	7.01	7.81	7.34	9.01	10.24	0.05	6.40	5.71	7.54	7.64	7.32	8.72	8.90	0.17
Na_2O	7.83	9.57	8.46	7.30	7.09	6.13	5.64	1.25	7.68	8.19	7.90	6.94	7.06	6.56	7.63	1.61
K_2O	0.20	0.41	0.17	0.10	0.18	0.13	0.07	14.42	0.32	0.42	0.10	0.12	0.11	0.11	0.12	13.97
Total	98.84	98.54	98.51	100.99	97.42	98.91	98.62	98.51	97.44	97.93	98.75	98.11	98.04	97.34	99.03	98.83
O	8.000	8.000	8.000	8.000	8.000	8.000	8.000	8.000	8.000	8.000	8.000	8.000	8.000	8.000	8.000	8.000
Si	2.704	2.675	2.665	2.638	2.658	2.539	2.516	2.992	2.687	2.697	2.649	2.635	2.635	2.654	2.629	2.994
Ti	0.001	0.003	0.001	0.001	0.001	0.000	0.000	0.001	0.000	0.001	0.001	0.001	0.001	0.001	0.000	0.001
Al	1.279	1.286	1.292	1.356	1.325	1.458	1.474	1.009	1.300	1.294	1.318	1.361	1.370	1.309	1.309	1.006
Fe	0.001	0.010	0.005	0.000	0.009	0.018	0.004	0.001	0.008	0.007	0.004	0.003	0.000	0.000	0.003	0.000
Mn	0.000	0.000	0.000	0.001	0.000	0.000	0.000	0.000	0.000	0.000	0.000	0.001	0.000	0.000	0.000	0.000
Mg	0.001	0.012	0.003	0.000	0.003	0.005	0.000	0.001	0.001	0.002	0.000	0.000	0.001	0.001	0.001	0.000
Ca	0.319	0.259	0.342	0.370	0.361	0.439	0.501	0.002	0.314	0.279	0.366	0.373	0.357	0.429	0.434	0.009
Na	0.684	0.845	0.747	0.626	0.630	0.540	0.499	0.116	0.682	0.723	0.695	0.613	0.623	0.585	0.673	0.146
K	0.012	0.024	0.010	0.006	0.011	0.007	0.004	0.879	0.019	0.024	0.005	0.007	0.006	0.007	0.007	0.836
Total	5.003	5.114	5.066	4.999	4.998	5.006	4.999	5.000	5.013	5.028	5.041	4.994	4.993	4.986	5.056	4.993
An	0.31	0.23	0.31	0.37	0.36	0.45	0.50	0.00	0.31	0.27	0.34	0.38	0.36	0.42	0.39	0.01
Ab	0.67	0.75	0.68	0.62	0.63	0.55	0.50	0.12	0.67	0.70	0.65	0.62	0.63	0.57	0.60	0.15
Or	0.01	0.02	0.01	0.01	0.01	0.01	0.00	0.88	0.02	0.02	0.01	0.01	0.01	0.01	0.01	0.84

Note: The letter 'inclusion' represents plagioclase inclusion enclosed within garnet core-mantle domains, while the 'core' and 'rim' represent core and rim of matrix-type plagioclase, and the 'fine' represents the symplectic plagioclase in the symplectites of biotite + sillimanite ± plagioclase ± quartz.

analysis in Supplementary Data Tables S3–S4 is reported in 1σ level, while mean ages for pooled U/Pb or Pb/Pb analyses are in 95% confidence.

The formation temperatures of zircons were calculated using Ti-in-zircon thermometer (Ferry and Watson, 2007). The presence of quartz suggests fully buffered SiO_2. Rutile is rare or absent in matrix. We thus set the activity of TiO_2 to 0.5 according to suggestion of Watson et al. (2006). The pressure effect on the thermometer was not calibrated. Based on zircon REE and inclusion characteristics, we suggest zircon formation or recrystallization at low pressure (< 10 kbar) within the sillimanite-stability field. Such low pressure has an insignificant effect on the calculated temperatures (Ferry and Watson, 2007). The Ti-in-zircon thermometry results are listed in Supplementary Table S5.

5. Mineral chemistry

The ratios or parameters characterizing compositional variations of minerals are Alm, Grs, Sps, Prp and X_{Mg} for garnet; TiO_2 content (wt %) and X_{Mg} for biotite; An, Or and Ab for feldspars; X_{Mg} for cordierite. They are defined as: Alm (almandine) = Fe^{2+} / (Fe^{2+} + Mg + Ca + Mn), Grs (grossular) = Ca / (Fe^{2+} + Mg + Ca + Mn), Prp (pyrope) = Mg / (Fe^{2+} + Mg + Ca + Mn), Sps (spessartine) = Mn / (Fe^{2+} + Mn + Mg + Ca) and X_{Mg} = Mg / (Mg + Fe^{2+}); An (anorthite) = Ca / (K + Na + Ca), Or (orthoclase) = K / (K + Na + Ca) and Ab

Table 3
Representative composition of cordierite from samples 17SD05, 17SD06 and 17SD07.

Sample	17SD07				17SD05			
Texture	Symplectite	Symplectite	Corona	Corona	Symplectite	Symplectite	Corona	Corona
SiO_2	48.83	48.70	48.51	48.82	46.57	48.79	48.92	49.02
TiO_2	0.02	0.02	0.02	0.00	0.00	0.00	0.00	0.00
Al_2O_3	33.46	33.28	33.55	33.28	33.87	33.21	33.01	33.26
FeO^T	6.45	6.75	6.01	6.60	7.41	6.67	5.85	7.00
MnO	0.01	0.02	0.03	0.05	0.08	0.06	0.04	0.06
MgO	9.64	9.15	9.90	9.38	7.78	9.31	9.80	8.76
CaO	0.03	0.00	0.05	0.04	0.07	0.02	0.05	0.00
Na_2O	0.05	0.06	0.04	0.07	0.19	0.05	0.17	0.06
K_2O	0.02	0.03	0.00	0.01	1.79	0.03	0.00	0.00
Total	98.53	98.03	98.13	98.26	97.79	98.15	97.88	98.17
O	18.000	18.000	18.000	18.000	18.000	18.000	18.000	18.000
Si	4.973	4.990	4.953	4.989	4.864	4.992	5.003	5.017
Ti	0.001	0.002	0.002	0.000	0.000	0.000	0.000	0.000
Al	4.016	4.019	4.038	4.008	4.170	4.005	3.979	4.011
Fe	0.549	0.579	0.513	0.564	0.647	0.571	0.500	0.599
Mn	0.001	0.002	0.002	0.004	0.007	0.005	0.004	0.005
Mg	1.464	1.398	1.507	1.429	1.212	1.419	1.494	1.337
Ca	0.003	0.000	0.006	0.004	0.008	0.003	0.005	0.000
Na	0.010	0.011	0.008	0.014	0.038	0.009	0.033	0.013
K	0.002	0.004	0.000	0.001	0.239	0.004	0.000	0.000
Total	11.023	11.006	11.030	11.014	11.188	11.010	11.022	10.983
X_{Mg}	0.727	0.707	0.746	0.717	0.652	0.713	0.749	0.691

Note: The symplectite means cordierite in the symplectites of cordierite + sillimanite.

(albite) = Na / (K + Na + Ca). Mineral abbreviations throughout the text follow Whitney and Evans (2010).

5.1. Garnet

Representative garnets are selected for compositional mapping (Fig. 7) and profile analysis (Fig. 8). All the analyzed garnets are Alm-Prp solid solutions, with minor Grs (< 0.1) and Sps (< 0.05). The Grs contents of garnet grains show a decreasing trend from core-mantle domains to the rim (Figs. 7a, e, i and 8). The Prp, Alm and Sps values are nearly homogenized throughout core-mantle domains (Fig. 7c–d, g–h, k–l, and o–p), with slight variations in the outermost rims mainly related to Fe-Mg exchange with matrix minerals during cooling (Fig. 7g, k, and o). In sample 17SD05, the Grs content ranges of garnet core, mantle, and rim domains are 0.044–0.050, 0.055–0.063, and 0.035–0.042, respectively. Garnet porphyroblasts in sample 17SD06 are generally euhedral (Fig. 5b) and their Grs values are characterized by

Table 5
Measured bulk-rock composition for phase modeling (mol%).

Sample	SiO_2	TiO_2	Al_2O_3	MgO	CaO	Na2O	K2O	O_2	FeO	H_2O
17SD05	64.12	0.67	13.92	6.24	1.35	0.93	2.6	0.11	8.74	1.32
17SD06	51.55	1.26	15.43	10.69	2.04	0.65	1.19	0.06	15.98	1.13
17SD07	60.73	0.95	14.54	6.78	3.2	2.24	1.25	0.06	9.12	1.11

Note: FeO is total Fe and O_2 is Fe_2O_3.

Table 4
Representative composition of biotite from samples 17SD05, 17SD06 and 17SD07.

Sample	16SD05					17SD06				17SD07			
Texture	Matrix	Matrix	Matrix	Inclusion	Inclusion	Inclusion	Inclusion	Matrix	Matrix	Inclusion	Inclusion	Matrix	Matrix
SiO_2	36.04	36.41	35.75	37.52	37.36	36.00	35.65	37.42	35.34	36.10	35.65	35.36	36.45
TiO_2	4.26	2.55	4.54	3.05	3.71	5.03	4.84	4.73	3.92	5.64	5.59	4.61	2.43
Al_2O_3	17.32	18.66	16.49	18.08	17.48	16.78	17.29	17.17	16.98	16.83	17.55	16.73	18.82
FeO^T	15.74	14.87	14.43	9.96	10.36	12.95	11.22	13.47	14.38	12.98	11.47	14.12	14.49
MnO	0.00	0.00	0.07	0.00	0.00	0.01	0.04	0.00	0.00	0.05	0.04	0.00	0.01
MgO	12.00	13.46	14.75	16.35	16.21	15.21	16.06	15.16	14.45	14.75	15.54	14.40	13.33
CaO	0.00	0.09	0.00	0.00	0.01	0.00	0.01	0.03	0.01	0.00	0.01	0.02	0.09
Na_2O	0.13	0.39	0.16	0.11	0.11	0.15	0.32	0.09	0.09	0.16	0.26	0.12	0.30
K_2O	9.64	9.23	10.42	9.98	10.04	10.35	10.30	9.34	10.28	10.10	10.17	10.70	9.42
Total	95.12	95.67	96.61	95.05	95.28	96.47	95.72	97.40	95.43	96.60	96.28	96.06	95.35
O	22.000	22.000	22.000	22.000	22.000	22.000	22.000	22.000	22.000	22.000	22.000	22.000	22.000
Si	5.406	5.392	5.300	5.470	5.454	5.298	5.250	5.403	5.296	5.297	5.219	5.275	5.409
Ti	0.481	0.284	0.506	0.335	0.408	0.557	0.536	0.513	0.442	0.623	0.615	0.518	0.271
Al	3.063	3.257	2.881	3.107	3.007	2.911	3.001	2.922	2.998	2.911	3.029	2.942	3.291
Fe	1.974	1.842	1.789	1.214	1.265	1.593	1.381	1.627	1.802	1.593	1.404	1.762	1.798
Mg	2.683	2.972	3.259	3.555	3.527	3.337	3.525	3.263	3.228	3.227	3.392	3.203	2.949
Mn	0.000	0.000	0.009	0.000	0.000	0.001	0.005	0.000	0.000	0.006	0.005	0.000	0.001
Ca	0.000	0.015	0.000	0.000	0.001	0.000	0.001	0.005	0.001	0.000	0.001	0.002	0.015
Na	0.037	0.112	0.047	0.032	0.031	0.042	0.090	0.024	0.025	0.044	0.075	0.034	0.086
K	1.846	1.744	1.971	1.856	1.870	1.943	1.935	1.720	1.964	1.891	1.900	2.035	1.784
Total	15.490	15.616	15.762	15.569	15.563	15.682	15.725	15.476	15.757	15.592	15.639	15.771	15.603
X_{Mg}	0.58	0.62	0.65	0.75	0.74	0.68	0.72	0.67	0.64	0.67	0.71	0.65	0.62

Note: The inclusion represents biotite inclusions within garnet mantle-core domains.

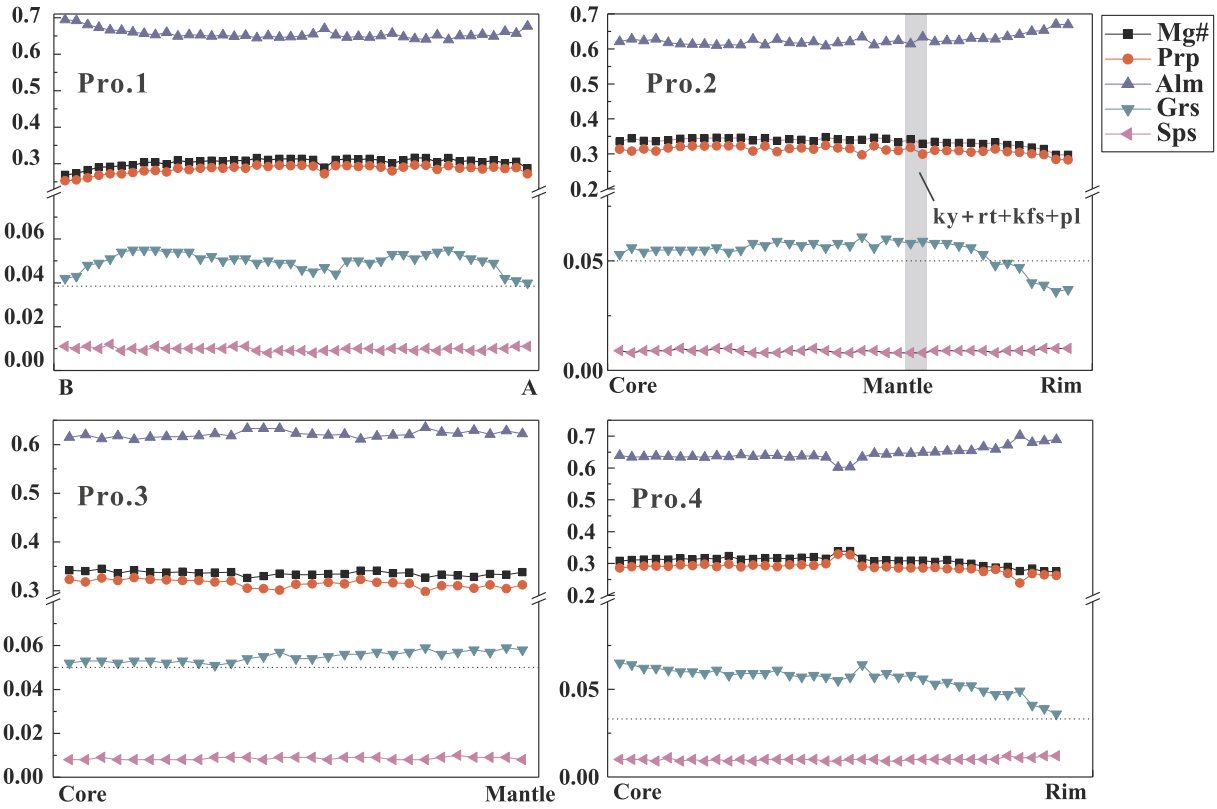

Fig. 8. Compositional profiles 1–4 for garnets shown in Fig. 7a, e, and i. The position of the polymineralic inclusions of kfs + ky + pl + rt + ilm is marked by projection to profile 2 shown in Fig. 7e.

an initial slight increase from the core (0.053–0.054) to the mantle (0.057–0.061), followed by a shape decrease to the rim of 0.036–0.043 (Fig. 7e; Fig. 8: Pros. 2 and 3). In sample 17SD07, relative euhedral garnets have a decreasing Grs from core domains (0.067–0.060) to the rim of 0.032–0.041 (Fig. 7i; Fig. 8: Pro. 4). In the cordierite-rich domains, garnets display embayed Grs zonation patterns similar to the corroded edges (Fig. 7m), with the lowest Grs contents of 0.035–0.030 measured from the outermost rims in contact with cordierite. The X_{Mg} values from garnet core-mantle and rim domains are 0.34–0.36 vs. 0.23–0.33, 0.34–0.35 vs. 0.30–0.32, and 0.31–0.35 vs. 0.28–0.29 for samples 17SD05, 17SD06, and 17SD07, respectively. In samples 17SD05 and 17SD07, garnet rims in contact with biotite + sillimanite ± quartz ± plagioclase have similar Grs contents, but slightly lower X_{Mg} values, compared with those rims surrounded by cordierite. We note that garnet mantle domains that enclose mineral inclusions of kyanite + rutile + K-feldspar + plagioclase + ilmenite have higher Grs contents than other domains (Figs. 6e–f and 7e–f).

5.2. Plagioclase

Coarse-grained matrix plagioclase is slightly zoned, with An contents of 0.30–0.35, 0.31–0.37, and 0.34–0.38 in the core, and of 0.35–0.41, 0.36–0.50, and 0.36–0.42 in the rim, for samples 17SD05, 17SD06 and 17SD07, respectively. The rare tiny plagioclase inclusions within garnet have slightly lower An contents, respectively being 0.27–0.28, 0.23–0.31, and 0.27–0.31 for samples 17SD05, 17SD06, and 17SD07. The fine-grained symplectitic plagioclase is compositionally similar to the rim of coarse-grained matrix plagioclase. Notably, the symplectic plagioclases near garnet rims have slightly higher An contents (e.g., up to 0.5 in sample 17SD06).

5.3. Cordierite

Cordierite coronae have slightly higher X_{Mg} values than those in symplectites of sillimanite + cordierite, being 0.69–0.75 vs. 0.65–0.71 and 0.72–0.75 vs. 0.71–0.73, respectively for samples 17SD05 and 17SD07. We note that the highest X_{Mg} value of cordierite is measured from grains adjacent to garnet rims, and slightly progressive Fe-enrichment away from the rim, possibly reflecting Fe-Mg exchange between cordierite coronae and garnet rims during cooling.

5.4. Biotite

We classify biotite into three groups: Bt_1, rounded biotite inclusions within garnet; Bt_2, relative coarse-grained biotite flakes in the matrix and Bt_3, fine-grained biotite in the symplectitic intergrowths of biotite + sillimanite ± plagioclase ± quartz. The Bt_1 is characterized by higher X_{Mg} values and relatively constant TiO_2 contents in comparison to the other two kinds. The Bt_1 has X_{Mg} values of 0.74–0.75, 0.68–0.72, and 0.67–0.71 for samples 16SD05, 16SD06, and 16SD07, respectively, with corresponding TiO_2 contents of 3.05–3.71%, 4.84–5.03%, and 5.64–5.59%. The other two kinds show little compositional variations among each sample, with X_{Mg} ranges of 0.58–0.65, 0.64–0.67, and 0.62–0.65, and TiO_2 ranges of 2.55–4.54%, 3.92–4.73%, and 2.43–4.61% for samples 16SD05, 16SD06 and 16SD07, respectively.

5.5. Rutile

In this study, we focus on the relatively well-preserved rutile inclusions within garnet. Rutile geochemistry shows wide ranges of Nd, Cr, and Zr contents (Supplementary Table S1). The Zr content ranges are 295–2300, 263–2439, and 285–2336 ppm respectively for samples 17SD05, 17SD06, and 17SD07. The pressure dependence Zr-in-rutile thermometer of Tomkins et al. (2007) was employed. The pressure was

set according to Grs contents of garnet, rutile stability in phase diagrams, and the GASP barometer (Holdaway, 2001) that used the core of matrix plagioclase or inclusion-type plagioclase. These constraints define a pressure range within 11–15 kbar that results in slight changes of Zr-in-rutile temperatures, and hence a median of ~13 kbar was chosen. The calculated temperatures show a wide range between 650 and 870 °C (Supplementary Table S1). Lower Zr-in-rutile temperatures (650–790 °C) are generally obtained from rutiles within garnet cores while those enclosed within garnet mantle domains have higher Zr-in-rutile temperatures (> 800 °C). This probably records a segment of prograde evolution during garnet growth from low temperature to peak metamorphism (Pauly et al., 2016). However, we also note some rutile inclusions within garnet mantles yield low Zr-in-rutile temperatures similar to those enclosed within garnet cores. Such rutiles are commonly associated with retrograde ilmenite. In this case, retrograde effect plays its role in scattering the Zr contents of rutile inclusions. Given that any retrograde reset lowers the Zr contents (Meinhold, 2010), the maximum measured Zr content should be regarded as the minimum estimation for rutile geochemistry at peak metamorphism (Zou et al., 2019). Therefore, the maximum Zr-in-rutile thermometry results of 860–870 °C obtained should be used as the lower limits for peak metamorphism.

6. Pseudosection modeling and geothermobarometry

Integrated approaches of pseudosection modeling and conventional geothermobarometry were employed to determine metamorphic *P-T* conditions. Pseudosection modeling in the NCKFMASHTO system was calculated by the Perple_X software version 6.7.8 (Connolly, 2005) and an internally consistent thermodynamic dataset of Holland and Powell (1998). We used the following mineral solutions: garnet, silicate melt (liq) and biotite (White et al., 2007); plagioclase and K-feldspar (Holland and Powell, 2003); muscovite and paragonite (Coggon and Holland, 2002); spinel and magnetite (White et al., 2002); ilmenite and hematite (White et al., 2000), and cordierite (Holland et al., 1998). Quartz, H_2O, and rutile were treated as pure phases. The measured bulk-rock compositions of relatively homogenous parts of the metapelites were used. The FeO contents were determined by chemical titration. The H_2O contents were constrained by the T-M_{H2O} pseudosections at appropriate pressures to ensure that the observed peak mineral assemblage is close to the solidus (Korhonen et al., 2013; Wei, 2016). The CaO contents were corrected on the basis of measured P_2O_5 contents. The normalized molar bulk compositions for pseudosection calculations are given in Table 5. Conventional geothermobarometry applied the GASP barometry (Holdaway, 2001), GB thermometry (Holdaway, 2000) and Zr-in-rutile thermometry (Tomkins et al., 2007).

6.1. Metamorphic P-T conditions of samples 17SD05 and 17SD07

The *P-T* pseudosections calculated for samples 17SD05 and 17SD07 are presented in Figs. 9 and 10 over a *P-T* range of 700–900 °C and 3–15 kbar. Quartz, ilmenite, and K-feldspar are predicted to be stable over the entire *P-T* range whereas the biotite is absent at $T > 820$ °C (Figs. 9a and 10a). The pseudosections are contoured with compositional parameters such as Grs and An contents (Figs. 9b and 10b), as well as X_{Mg} in garnet and cordierite and garnet volume percentage (Figs. 9c–d and 10c–d). Based on inclusions within garnet cores, we place the prograde M_1 stage at rutile-, kyanite-, and biotite-stability fields. The euhedral garnet has a Grs increase from core to mantle domains (Fig. 7a–d), which predicts a prograde path featured by an increase in pressure and temperature (Figs. 9b and 10b). The peak M_2 assemblage is modeled in the fields of bt-liq-pl-grt-ky-rt and liq-pl-grt-ky-rt at $T > 800$ °C, $P > 10$ kbar (Figs. 9a and 10a). Integration of the highest measured Grs from garnet core-mantle domains and the lowest An contents measured from plagioclase inclusions within garnet yields $T \geq 810$ °C, $P \geq 11$ kbar. The upper limit in temperature cannot be well constrained by phase modeling. The GASP barometer applied to the garnet core-to-mantle domains and the cores of matrix plagioclase, in concert with Zr-in-rutile thermometry, suggests minimum *P-T* conditions of ~860 °C, ~13 kbar (Figs. 9b and 10b).

The observed M_3 assemblage is predicted in the field of liq-crd-pl-grt-sil (Figs. 9a and 10a). The *P-T* conditions of the M_3 stage can be broadly constrained to ~6.5 kbar, > 840 °C using average X_{Mg} values of symplectic cordierites (X_{Mg} = ~0.70 for sample 17SD05 and X_{Mg} = ~0.73 for sample 17SD07; Figs. 9c and 10c) and Grs contents of garnet rims. The maximum temperature cannot be fully constrained by phase modeling because robust compositional isopleths like garnet mode and An and Grs contents are nearly parallel to the temperature axis (Figs. 9b–d and 10b–d). The metamorphic *P-T* path from the M_2 to M_3 stages cuts across the kyanite/sillimanite and rutile/ilmenite transformation and cordierite-out lines (Figs. 9a–b and 10a–b), consistent with observed kyanite pseudomorphed by sillimanite (Fig. 4d and f), replacement of rutile by ilmenite, and formation of cordierite, pointing to a decompression process. Since no spinel or orthopyroxene has been observed, the possible temperature increase during decompression may be insignificant and hence we tentatively consider the decompression as essentially isothermal.

The retrograde M_4 assemblage is not fully in equilibrium with the rest of the matrix and thus cannot be quantitatively mapped in the phase diagram. The GB and GASP thermobarometers applied to the outermost garnet rims and nearby symplectic biotite and plagioclase define *P-T* conditions of 4–6 kbar and ~600 °C (Figs. 9b and 10b). The *P-T* path from the M_3 to M_4 stages is featured by a near isobaric cooling (Figs. 9b and 10b).

6.2. Metamorphic P-T conditions of sample 17SD06

The *P-T* phase modeling of sample 17SD06 is shown in Fig. 11, with quartz, ilmenite, and K-feldspar modeled to be stable over the *P-T* range of interest. Similar to samples 17SD05 and 17SD07, the prograde M_1 assemblage occurs in the biotite-, rutile-, and kyanite-stability fields. The Grs contents in garnet core domains suggest a prograde path that is characterized by temperature and pressure increases evolving to the peak M_2 conditions (Fig. 11b). The peak M_2 assemblage is predicted in the field of bt-liq-pl-grt-ky-rt or liq-pl-grt-ky-rt (Fig. 11a). The highest measured Grs contents of ~0.061 from garnet mantle domains that enclose polymineralic inclusions of kyanite + rutile + K-feldspar + plagioclase + ilmenite (Figs. 6e–f and 7e–f) and the lowest An contents of ~0.23 from plagioclase inclusions constrain *P-T* conditions to > 12 kbar, > 810 °C. The combined Zr-in-rutile thermometer and GASP barometer (applied to garnet mantle domains and associated plagioclase inclusions) yield *P-T* conditions of ~870 °C, 13–14 kbar (Fig. 11b).

The post-peak M_3 stage is characterized by transformation of kyanite to sillimanite and rutile to ilmenite. Garnet zonation reveals a decrease in Grs contents from mantle to rim domains (Fig. 7e), associated with zoned matrix plagioclase grains displaying a rim-ward increase in An contents. These compositional variations reflect the equilibria reaction: grossular + aluminosilicate + quartz = anorthite, implying a significant decompression process from the M_2 to M_3 stages (Fig. 11b). The Grs contents of ~0.042 from garnet rims and the average An content of ~0.47 from matrix plagioclase rims yield possible *P-T* conditions at ~7 kbar, > 840 °C (Fig. 11b). The maximum temperature at this stage cannot be constrained by phase modeling. Similar to cordierite-bearing samples, we consider the decompression process as near isothermal (Fig. 11b). We note that some measured Grs contents from garnet rims (e.g., Grs = 0.36) and An contents from matrix plagioclase rims (e.g., An = 0.45–0.50) are predicted in lower pressure domains where cordierite becomes stable (P = 4–5.5 kbar; Fig. 11b), which is inconsistent with the fact that no cordierite is observed. The contradiction may be explained by the uncertainties of pseudosection modeling (e.g., Palin et al., 2016), or that cordierite

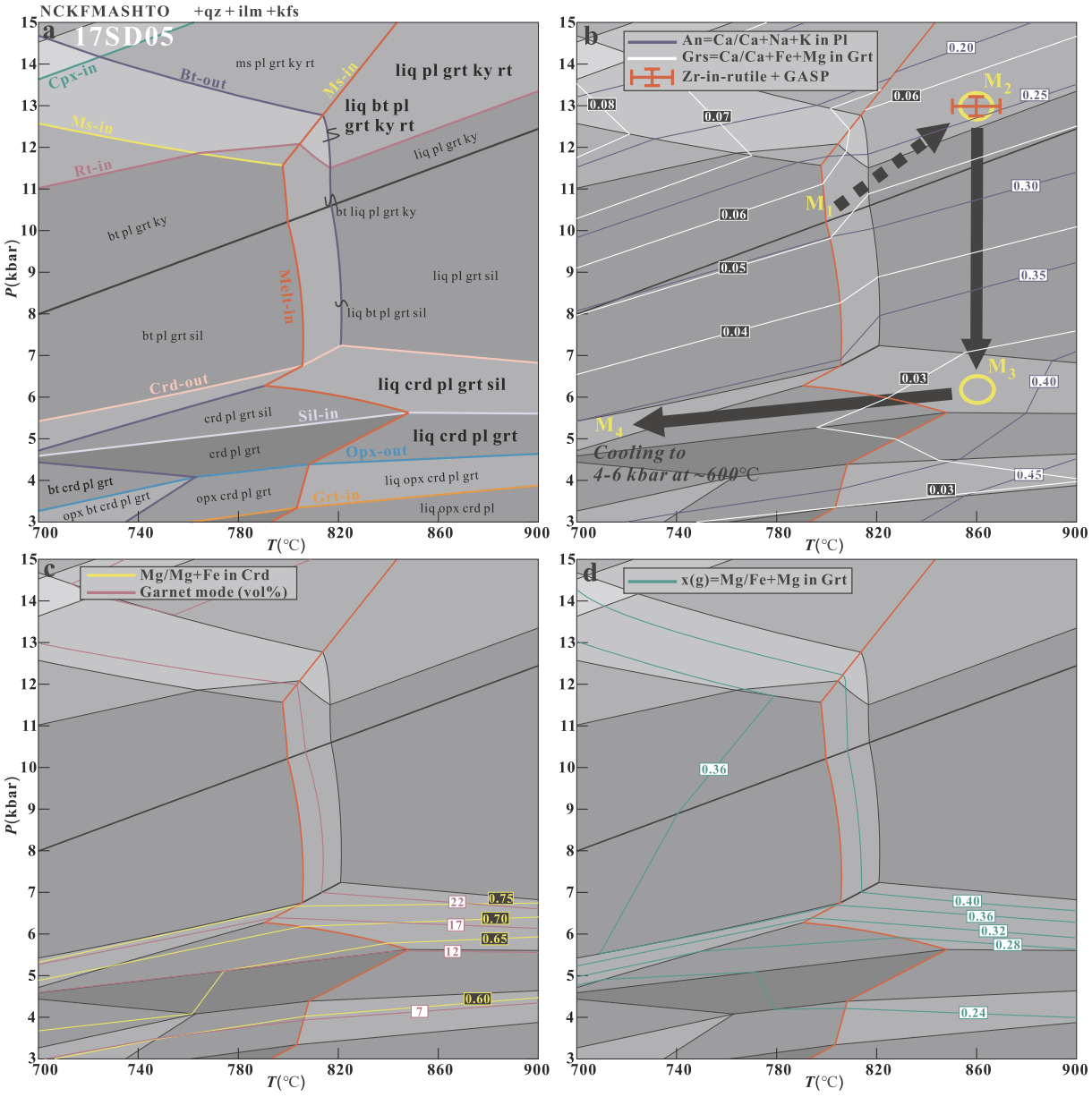

Fig. 9. *P-T* pseudosections computed using measured bulk-rock composition for sample 17SD05. Phase diagrams labeled with (a) modeled phase assemblages and boundaries, (b) isopleths of Grs and An, (c) X_{Mg} in cordierite and garnet mode (vol %), and (d) X_{Mg} in garnet. The yellow circles denote approximate *P-T* conditions for each metamorphic stage. The final *P-T* conditions of 4–6 kbar, ~600 °C for the M_4 stage are estimated by the GB and GASP thermobarometers (Holdaway, 2000, 2001). The thick black lines represent the likely *P-T* path. See text for details. (For interpretation of the references to color in this figure legend, the reader is referred to the web version of this article.)

formation during decompression is controlled by kinetics rather than thermodynamics. The final equilibrium *P-T* conditions for the M_4 stage is determined at ~600 °C, 4–6 kbar using the GB and GASP thermobarometers on outermost garnet rims and nearby symplectic biotite and plagioclase, suggesting near isobaric cooling (Fig. 11b).

7. Geochronology

The timing of metamorphism is constrained by performing monazite and zircon U-Pb geochronology on samples 17SD06 and 17SD07. The results are briefly summarized below.

7.1. Zircon geochronology

Zircon grains separated from sample 17SD06 are oval-rounded and ~100 μm in size. Most grains range from unzoned to exhibiting sector zoning in CL images (Fig. 12a), while a minority of grains have a core-rim texture featuring a CL-dark core and a CL-bright rim that is too narrow to be accurately analyzed (Fig. 12a: spots 1, 11 and 18). The core is unzoned and the core-rim boundaries are curved and display dissolution textures, indicating that the CL-bright rims are newly-grown metamorphic zircons most likely formed through intergranular melt (Zhao et al., 2015). The dominant unzoned to sector zoning zircon crystals have CL luminance similar to those of the CL-bright rims. A total of 24 analyses (five analyses on the CL-dark cores) were conducted on 24 zircon grains. These 24 analyses have U and Th contents of 139–710 and 6–18 ppm, yielding low Th/U ratios of 0.01–0.07 suggestive of metamorphic origin (Vavra et al., 1996). The 24 analyses plot along the concordia line (Fig. 13a). Except one spot (Fig. 12a: spot 22) yielding an older apparent $^{207}Pb/^{206}Pb$ age of 1978 ± 24 Ma (Fig. 13a), the rest of 23 analyses have apparent $^{207}Pb/^{206}Pb$ ages of 1818–1875 Ma, defining a weighted mean of 1851 ± 10 Ma (Fig. 13a).

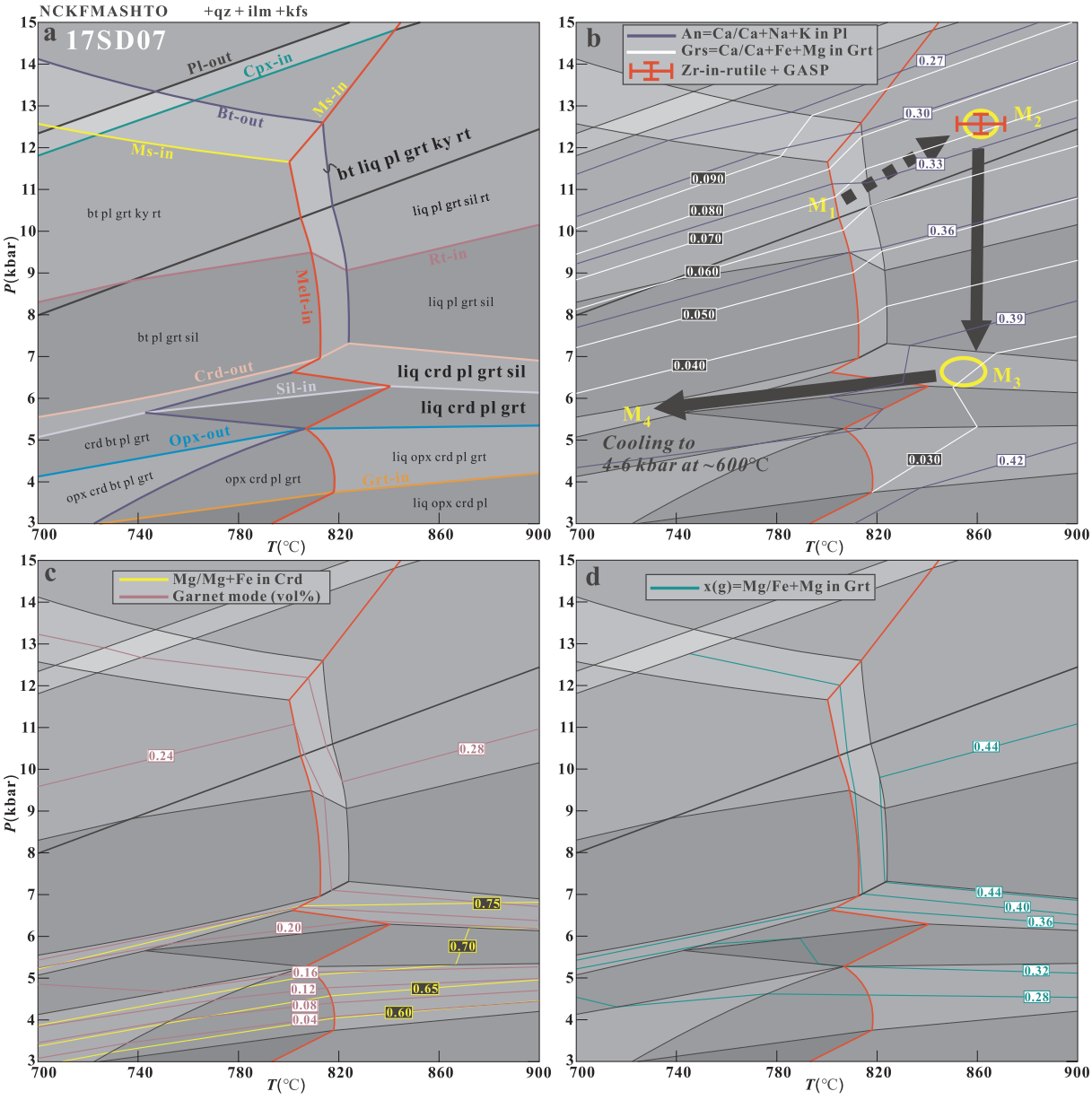

Fig. 10. *P-T* pseudosections calculated with measured bulk-rock composition for sample 17SD07. *P-T* pseudosections marked with (a) modeled phase assemblages and boundaries, (b) isopleths of Grs and An, (c) X_{Mg} in cordierite and garnet mode (vol %), and (d) X_{Mg} in garnet. The yellow circles denote approximate *P-T* conditions for each metamorphic stage. The final *P-T* conditions of 4–6 kbar, ~600 °C are determined by the GB and GASP thermobarometers (Holdaway, 2000, 2001). The thick black lines show the possible *P-T* path. See text for details. (For interpretation of the references to color in this figure legend, the reader is referred to the web version of this article.)

Zircon REE contents shows that all analyses have negative En anomalies (Eu/Eu* = 0.09–0.53, average = 0.22), low HREE contents, and flat HREE patterns (Lu_N = 6–121, average = 29; Lu_N/Gd_N = 0.08–2.22, average = 0.47; Fig. 14c).

Zircons from sample 17SD07 are rounded to rectangle and 50–150 μm in size (Fig. 12b). Their CL characteristics are similar to those of sample 17SD06. A total of 24 analyses (six on the CL-dark cores) were performed on 24 grains. They display a slight variation in Th (5–43 ppm) and U contents (130–1055 ppm), but yield consistently low Th/U ratios (0.01–0.09). The 24 analyses are concentrated on the concordia line, giving apparent $^{207}Pb/^{206}Pb$ ages of 1810–1921 Ma and a weighted mean of 1846 ± 9 Ma (Fig. 13b). These analyses (except spot 18) are characterized by negative En anomalies (Eu/Eu* = 0.08–0.75, average of 0.26) and flat HREE patterns (Lu_N = 8–280; Lu_N/Gd_N = 0.11–5.36, average of 0.67; Fig. 14d).

We notice that the zircon CL-dark cores also record similar ages of ~1.85 Ga (Fig. 12a: spot 11; 12b: spot 17). Most of these cores display indistinguishable REE characteristics and Ti-in-zircon thermometry results (720–760 °C) from the unzoned to sector zoning zircon crystals (Fig. 14c–d; Supplementary Table S5). If these cores originated as pre-metamorphic grains, their U-Pb systems and REE contents have been completely reset most likely by solid-state recrystallization coupled with dissolution (Geisler et al., 2007; Schaltegger et al., 1999; Zhao et al., 2015).

7.2. Monazite geochronology

Monazite grains from sample 17SD06 are rounded to irregular in shape and 100–200 μm in size (Fig. 12c). BSE images reveal a homogenous internal texture (Fig. 12c). A total of 20 spots were made from 16 grains. The 20 spots have U and Th contents ranging between 0.16 and 0.94 and 3.4–5.4 wt%, respectively, yielding an apparent

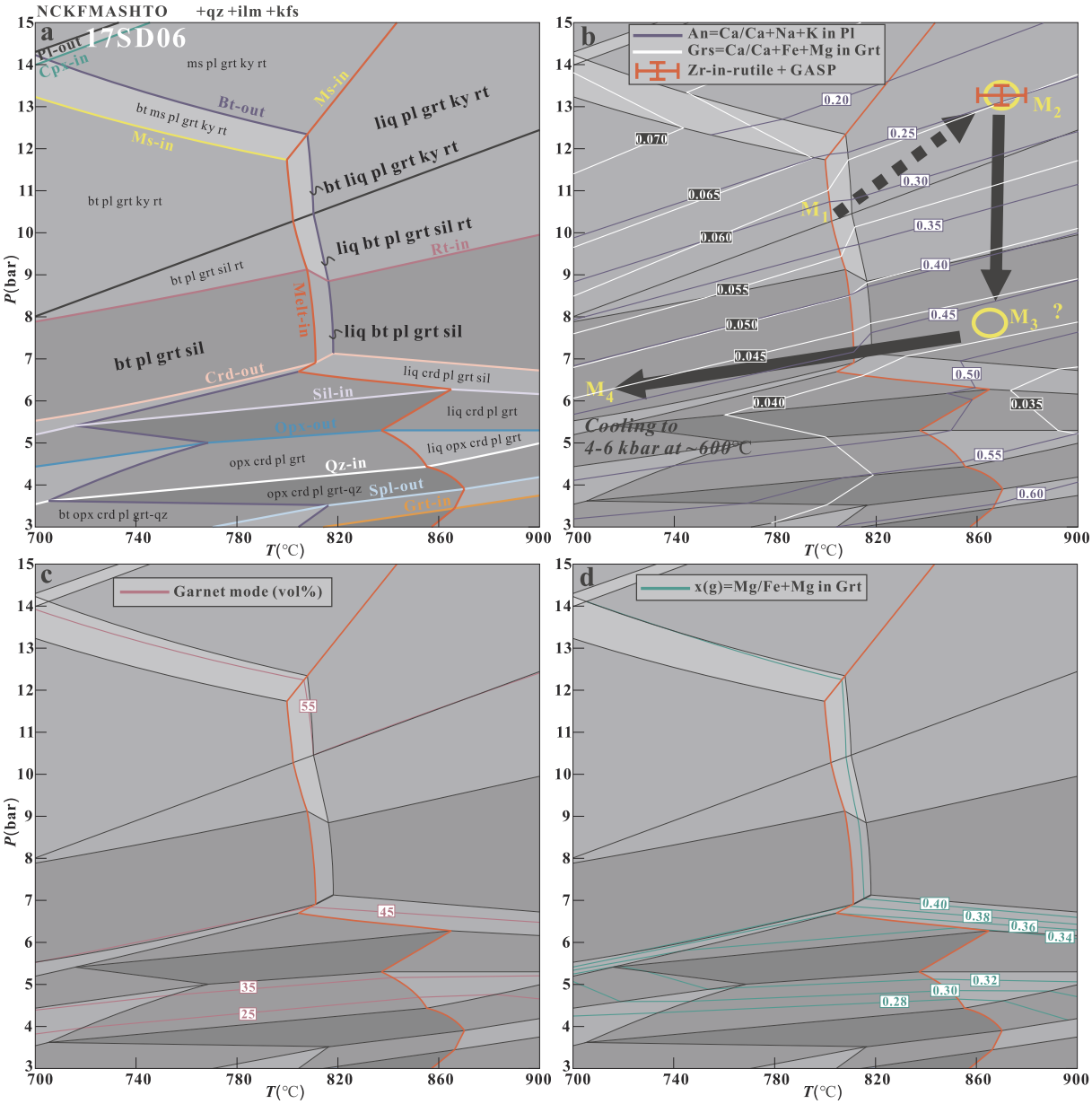

Fig. 11. *P-T* phase modeling of sample 17SD06 using measured bulk-rock composition. *P-T* phase diagrams marked with (a) modeled phase assemblages and boundaries, (b) isopleths of Grs and An, (c) garnet mode (vol %), and (d) X_{Mg} in garnet. The yellow circles denote approximate *P-T* conditions for each metamorphic stage. The GB and GASP thermobarometers give final *P-T* conditions of 4–6 kbar, ~600 °C (M_4 stage). The thick black lines represent the possible *P-T* path. See text for details. (For interpretation of the references to color in this figure legend, the reader is referred to the web version of this article.)

$^{207}Pb/^{206}Pb$ age range of 1833–1870 Ma. Among the 20 spots, 18 analyses with < 1% discordance give a concordia age of 1849 ± 6 Ma (Fig. 13c).

Monazite grains extracted from sample 17SD07 are homogenous, 100–200 μm in size, and rounded to irregular in shape (Fig. 12d). Metamorphic mineral sillimanite is identified within monazite (Fig. 12d: spot 25), suggesting formation in the sillimanite-stability field. Twenty-five spots were analyzed from 21 grains. They have U and Th contents and Th/U ratios of 0.16–0.69 wt%, 4.0–5.6 wt%, and 4–31, respectively. The 25 analyses are concentrated on the concordia line (Fig. 13d), of which 16 analyses with < 1% discordance yield a concordia age of 1858 ± 6 Ma (Fig. 13d).

8. Discussion

8.1. Metamorphic P-T-t evolution of pelitic granulites

In this study, we identify kyanite relics and the mineral assemblage of kyanite + K-feldspar + rutile + garnet from typical cordierite/sillimanite-bearing LMP pelitic granulites. Integrated approaches of petrology, phase modeling, and geothermobarometry reveal an earlier HP granulite-facies metamorphism, with minimum *P-T* conditions of 860–870 °C, 13–14 kbar (M_2 stage; Figs. 9b, 10b and 11b). Subsequently, these rocks underwent near isothermal decompression to 4–7 kbar, > 840 °C (M_3 stage) and experienced LMP granulite-facies retrogression. During this retrograde metamorphism, the cordierite-bearing metapelites witnessed cordierite formation while the garnet-rich metapelites did not. The reason for the absence of cordierite is out of scope of this paper and requires further study. We note that the upper

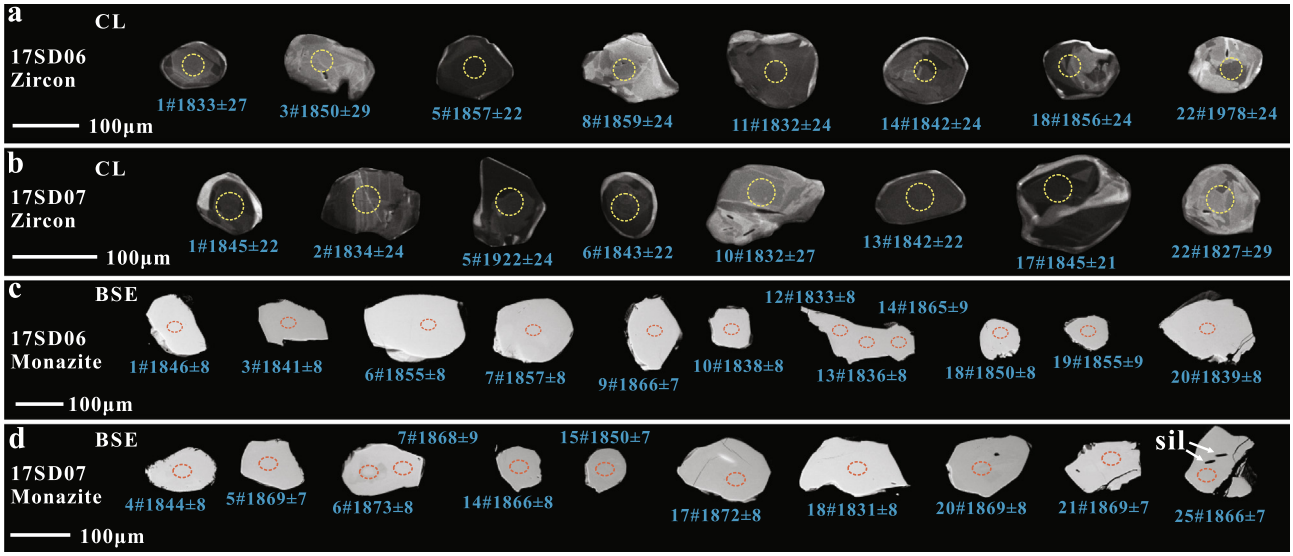

Fig. 12. Representative CL images of zircons and BSE images of monazites. Dash yellow circles denote the LA-ICP-MS analysis spots of ~32 μm diameter while dash red ellipses represent the SIMS analysis spots in size of 30 × 20 μm. The blue numbers indicate the spot number and the apparent $^{207}Pb/^{206}Pb$ age with error (1σ). (For interpretation of the references to color in this figure legend, the reader is referred to the web version of this article.)

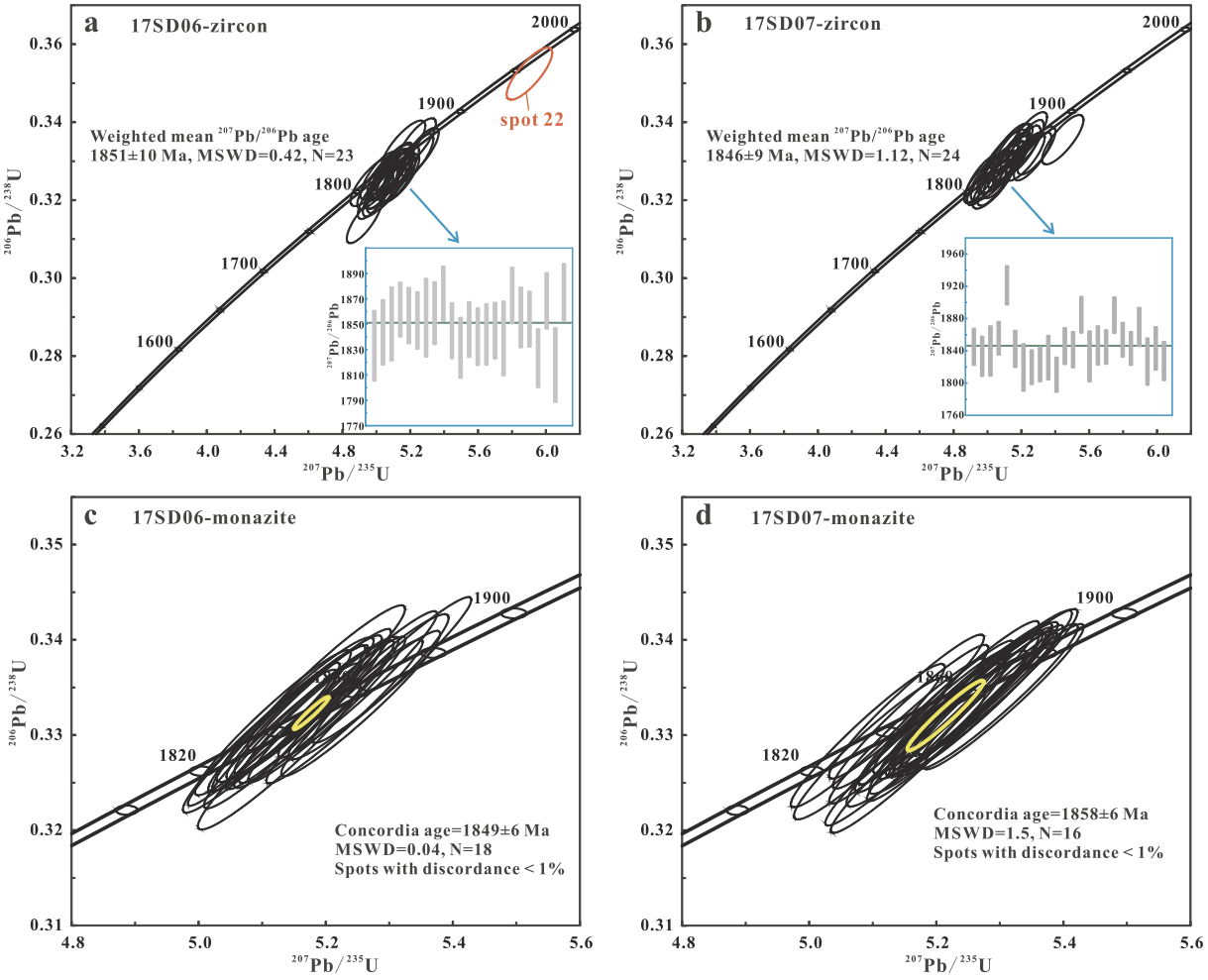

Fig. 13. Zircon and monazite U-Pb concordia diagrams.

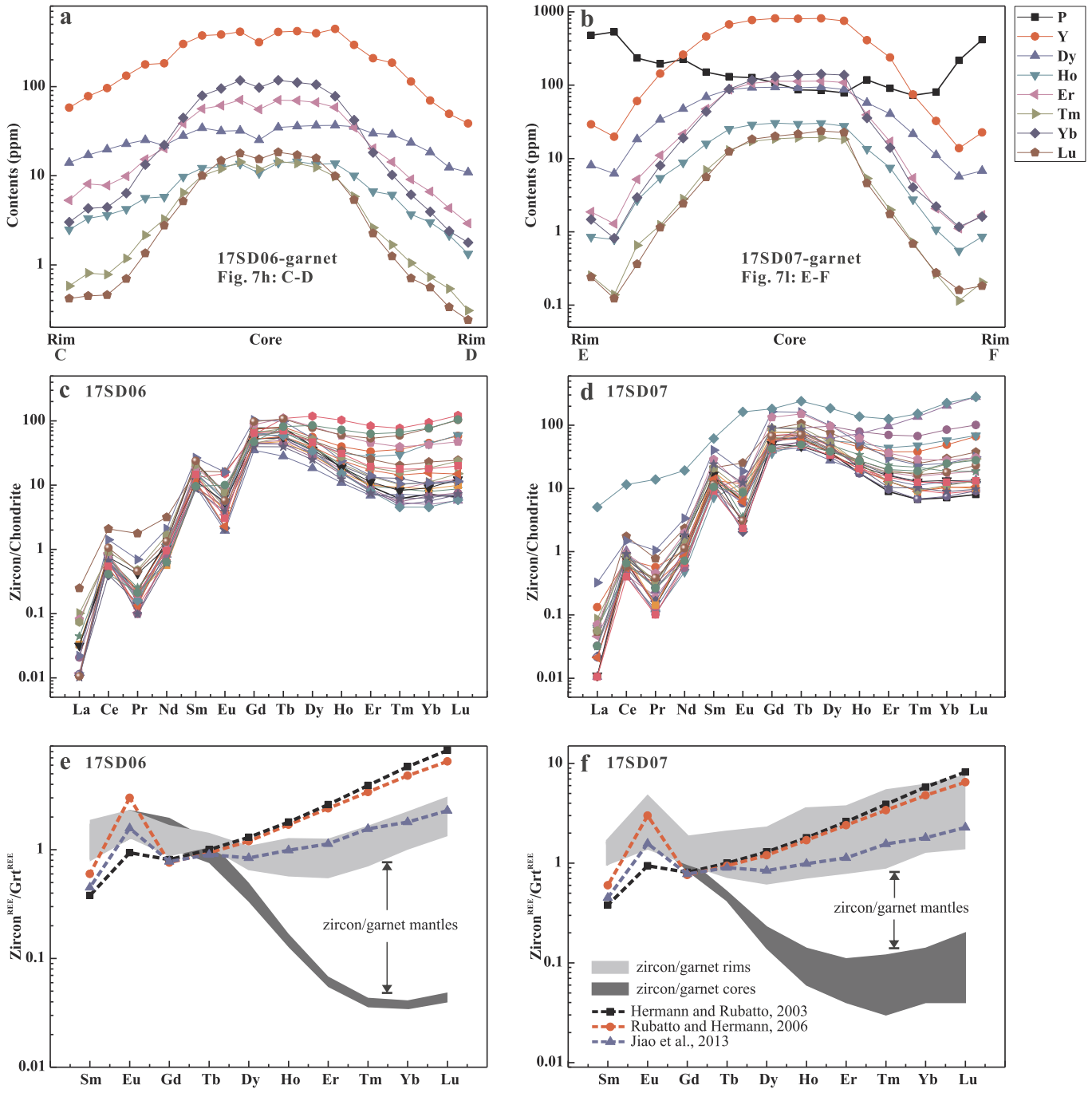

Fig. 14. (a–b) REE zoning profiles of garnet traverses C-D and E-F shown in Fig. 7h, l. (c–d) Zircon chondrite-normalized REE patterns for samples 17SD06 and 17SD07. Chondrite REE values are from Sun and Mcdonough (1989). (e–f) Partition coefficients calculated for MREE-HREE between zircon and garnet. The zircon/garnet rims and the zircon/garnet cores mean that averaged value of zircon grains verses values from garnet rims and cores, respectively. The distribution coefficients estimated by Hermann and Rubatto (2003) from pelitic granulites, by Rubatto et al. (2006) from low-pressure metapelitic diatexite and by Jiao et al. (2013) from UHT pelitic granulites are shown for comparison.

temperature limit for the M_3 stage is not well constrained. Based on petrographic observations, this stage proceeded at high-temperature conditions where biotite is unstable. The *P-T* evolution subsequent to M_3 stage is characterized by near isobaric cooling to final *P-T* conditions of ~600 °C, 4–6 kbar, documented by biotite + sillimanite ± plagioclase ± quartz symplectites (M_4 stage).

Zircon and monazite give indistinguishable ages of ~1.85 Ga (Fig. 13). Mineral inclusions of sillimanite identified within monazite grains (Fig. 12d: spot 25) constrain the ~1.85 Ga age as representative of metamorphism within the sillimanite-stability field rather than the peak pressure stage (M_2). The flat HREE patterns of zircon suggest their formation in the presence of garnet (Fig. 14c–d; Hermann and Rubatto, 2003; Rubatto and Hermann, 2006; Schaltegger et al., 1999; Wu et al., 2008). The calculated HREE partition coefficients between garnet and zircon imply that most metamorphic zircons formed in equilibrium with garnet rims (Fig. 14e–f). This relates the ~1.85 Ga age to the M_3-M_4 metamorphic stages. In addition, Ti-in-zircon thermometry gives formation temperatures mainly in the range of 720–760 °C (Supplementary S5), which are lower than the $T > 840$ °C expected for the M_3 stage. Given the diffusivity of Ti in zircon is extremely slow

(Cherniak and Watson, 2007), the low Ti-in-zircon thermometry results did not likely result from diffusive resetting. This may instead imply that zircon growths or recrystallization was delayed until a cooling process from the M_3 stage occurred. This delay effect has been modeled in recent thermodynamic simulations, which suggests that zircon and monazite tend to dissolve into melt at high-temperature, but are prone to crystallize upon melt crystallization during cooling (Kelsey et al., 2008; Kelsey and Powell, 2011). We note, however, that the current Ti-in-zircon thermometers cannot always truthfully reflect the crystallization temperature (Siegel et al., 2018) and can in some instances yield lower temperature estimates (Fu et al., 2008). Besides, in high-grade rocks, monazite and zircon that yield similar ages are generally interpreted to suggest equilibrium close to peak conditions (e.g., Rubatto et al., 2006). Therefore, considering the above lines of evidence, we interpret the ~1.85 Ga age as the timing of high-temperature LMP granulite-facies retrogression likely within 720–760 °C after a cooling from the M_3 stage. This interpretation is compatible with previous geological data. Metamorphic ages of ~1.85 Ga have also been reported from HP granulites elsewhere in the Jiaobei terrane. These ages have been interpreted to date the decompression and cooling stages of HP granulites, reflecting hot exhumation and cooling during orogenic collapse of the JLJB (Liu et al., 2013c, 2015c; Zou et al., 2019). Hot exhumation and subsequent cooling processes resulted in pervasive LMP granulite-facies retrogression (Lee et al., 2018; Liu et al., 2011b, 2013c, 2015a, 2015c; Tam et al., 2011), widespread partial melting, and migmatization along the JLJB (Liu et al., 2014, 2017a).

It is worth mentioning that one zircon U-Pb analysis yields an older apparent $^{207}Pb/^{206}Pb$ age of 1978 ± 24 Ma (Fig. 12a: spot 22; Fig. 13a). This spot has CL and REE characteristics and a Ti-in-zircon thermometry result indistinguishable from the unzoned to zoned zircon crystals (Supplementary Table S5), suggesting a metamorphic origin. Relating this metamorphic U-Pb age to a specific metamorphic stage may be unreliable. Nevertheless, it is noted that the timing of the HP granulite-facies metamorphism in the Jingshan Group has been constrained to 1950–1890 Ma by recent studies (e.g., Liu et al., 2013c, 2015a, 2017b; Tam et al., 2011; Zou et al., 2019). Based on these geochronological data, we tentatively consider the 1978 ± 24 Ma as dating metamorphism close to the peak pressure of the M_2 stage. We notice that 1.95–1.90 Ga metamorphic ages have been commonly reported from Paleoproterozoic HP granulites elsewhere in the NCC (Zhou et al., 2017), but are very rare in our samples. The scarcity of 1.95–1.90 Ga metamorphic ages, as well as the rare occurrence of kyanite, in the typically cordierite/sillimanite-bearing LMP pelitic granulites of the Jingshan Group, is most likely due to the extensive retrograde modification by the LMP granulite-facies metamorphism at ~1.85 Ga. Consequently, a metamorphic *P-T-t* path from these cordierite/sillimanite-bearing LMP pelitic granulites is defined that suggests an earlier HP granulite-facies metamorphism of 860–870 °C, 13–14 kbar possibly at ~1.95 Ga, followed by near isothermal decompression to 4–7 kbar, > 840 °C and subsequent isobaric cooling at ~1.85 Ga, with final equilibrium *P-T* conditions of ~600 °C, 4–6 kbar (Fig. 15).

8.2. Relationship between LMP and HP pelitic granulites

Regional pelitic granulites in many ancient high-grade terranes worldwide are pervasively dominated by LMP granulites, featured by cordierite/sillimanite-bearing assemblages (e.g., Harley, 1989; Liu et al., 2019; Lu et al., 1996; Prakash, 1999; Tam et al., 2012a; Turkina and Sukhorukov, 2015; Yan et al., 1991). For a given region when even HP pelitic granulites have been reported, the exposures are very limited. The relationship between the rare HP pelitic granulites and the dominant LMP pelitic granulites remains elusive, and whether the dominant LMP types are retrograde products of the HP ones remains a topic of controversy. This uncertainty limits a full understanding of the spatial distribution of HP pelitic granulites and the nature of corresponding lithospheric processes in deep time.

In this study, we consider typically cordierite/sillimanite-bearing

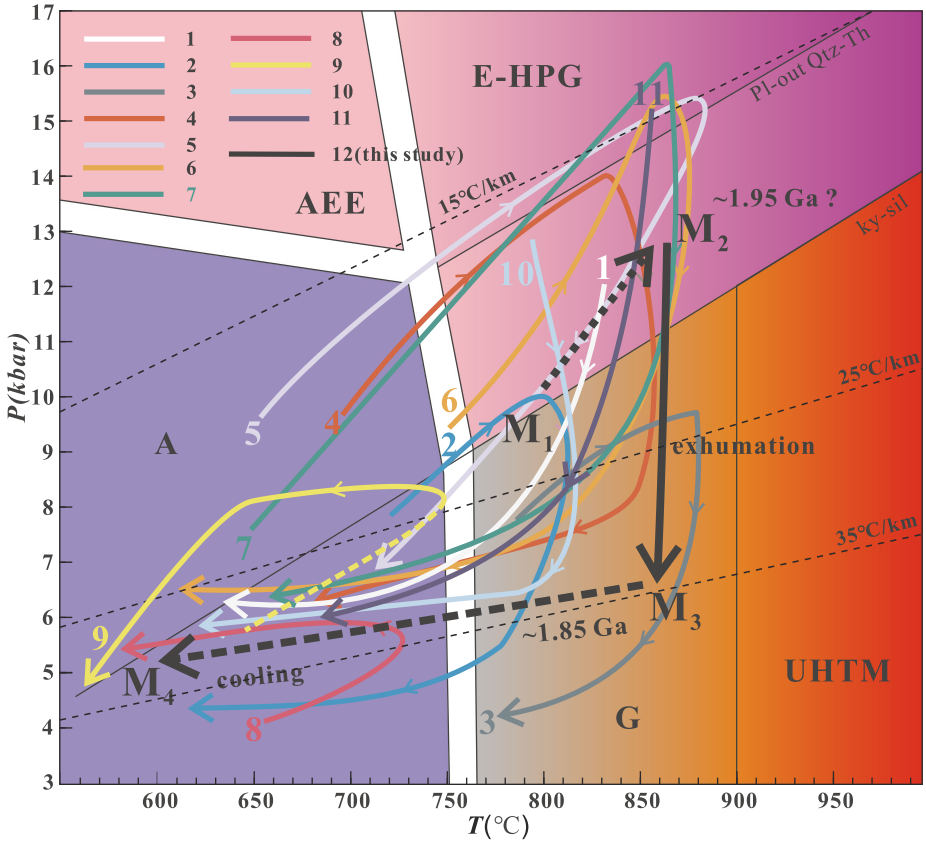

Fig. 15. Reported metamorphic *P-T-t* paths from the Jiaobei terrane. Summarized data are: path 1 (Zhou et al., 2004); path 2 (Wang et al., 2010); path 3 (Tam et al., 2012a); path 4 (Tam et al., 2012b); path 5 (Tam et al., 2012c); path 6 (Liu et al., 2013c); path 7 (Zou et al., 2017); path 8 (Lu et al., 1996); path 9 (Zou et al., 2018); path 10 (Liu et al., 2017b), path 11 (Zou et al., 2019) and path 12 (this study; sample 17SD07). Metamorphic facies and boundaries follow Brown (2014). E-HPG, eclogite- to high-pressure granulite-facies; UHTM, ultrahigh-temperature metamorphism; G, granulite-facies; A, amphibolite-facies and AEE, amphibole-epidote eclogite facies.

LMP pelitic granulites from the Jiaobei terrane, and identify kyanite relics and a mineral assemblage suggestive of an earlier HP granulite-facies metamorphism. These findings demonstrate that at least some portions of LMP pelitic granulites within the Jiaobei terrane are retrograded from the HP pelitic granulites. The later LMP granulite-facies retrogression during exhumation and cooling processes at ~1.85 Ga eclipsed the earlier HP granulite-facies records. Our results thus greatly expand the spatial distribution of HP pelitic granulites, which in concert with the HP mafic granulites (Liu et al., 2017b) constitute a linear HP granulite-facies metamorphic belt along the Pingdu-Laiyang areas of the Jiaobei terrane (Fig. 1c). The linear distribution pattern renders the overpressure model unlikely (Zou et al., 2019), and requires geodynamic processes similar to those operative in modern convergent plate margins.

We suggest that the cordierite/sillimanite-bearing LMP pelitic granulites that have kyanite relics serve as 'intermediate products', providing mineralogical evidence to confirm that at least some portions of the LMP pelitic granulites are retrograded from the typical HP ones without cordierite. The existence of such intermediate products helps to restore the original spatial distribution of ancient HP pelitic granulites and evaluate the nature of corresponding tectonic processes in deep time. The potential of identifying kyanite relics and an earlier stage of HP granulite-facies metamorphism in typically cordierite/sillimanite-bearing LMP pelitic granulites should not be overlooked, and can be applied to many other Precambrian high-grade terranes worldwide where pelitic granulites are dominated by LMP types.

8.3. Implications for tectonic evolution of the JLJB

The JLJB has witnessed a very complex Paleoproterozoic tectonic history including massive deposits of volcanic and sedimentary materials and multi-stage magmatic-metamorphic events (Liu et al., 2015a; Xu and Liu, 2019; Yang et al., 2019). Geodynamic processes involved in the formation of the JLJB harbor clues for revealing tectonic regimes in relation to the assembly of supercontinent Columbia/Nuna (Evans and Mitchell, 2011). Over the past two decades, extensive geochronological, geochemical, magmatic, sedimentological, metamorphic, structural and geophysical studies have been conducted that provide a huge amount of new data (see reviews by Liu et al., 2015a; Xu and Liu, 2019; Yang et al., 2019), contributing to a better understating on tectonic history of the JLJB. Nevertheless, the detailed tectonic processes responsible for the formation of the JLJB are still a subject of debate, and several tectonic models have been proposed. These tectonic models mainly include: (1) continental rift model, initially proposed by Zhang and Yang (1988) and Zhang (1984), which has been refined and substantiated by subsequent studies (e.g.Li and Zhao, 2007; Li et al., 2006; Luo et al., 2004, 2008; Peng et al., 2016; Wang et al., 2017c; Zhao et al., 2005); (2) various versions of continent-arc-continent collision models with different subduction polarities (e.g., Bai, 1993; Faure et al., 2004; Li and Chen, 2014; Peng et al., 2014; Wang et al., 2017a) or divergent double subduction (Yuan et al., 2015); (3) closure of back-arc basin or *retro*-arc basin models (e.g., Kusky et al., 2016; Li et al., 2018; Meng et al., 2014; Xu et al., 2018b; Yang et al., 2019; Zhang et al., 2018). Notably, recent new metamorphic data particularly the metamorphic *P-T-t* paths from HP granulites within the Jiaobei terrane have made a reversion to the continental rift model. The revised continental rift model suggests that even though the JLJB originated as a continual rift, it developed into an oceanic basin, with eventual closure of the ocean basin through subduction and collision (e.g., Liu et al., 2015c; Peng et al., 2016; Tam et al., 2012b, 2012c; Wang et al., 2010; Zhou et al., 2004, 2008b; Zou et al., 2017, 2019). It is difficult to adopt any of these models. We note that each model is supported by abundant geological data and does not fully conflict with the others, implying spatial and temporal complexity and variability in the geological records during the evolution of the JLJB (Xu and Liu, 2019).

In this contribution, we provide petrographic evidence to show that at least some portions of the typically cordierite/sillimanite-bearing LMP pelitic granulites are retrograded from HP pelitic granulites, implying a linear distribution of HP pelitic granulites within the Jiaobei terrane. The defined clockwise *P-T-t* path from these LMP pelitic granulites is similar to those reported from HP pelitic and mafic granulites elsewhere in the Jiaobei terrane (Fig. 15; Liu et al., 2015c, 2017b; Tam et al., 2012b, 2012c; Zhou et al., 2004, 2008b; Zou et al., 2017, 2019), indicating that they experienced a common tectothermal event. Similar clockwise *P-T* paths associated with HP granulite-facies metamorphism are retrieved from metamorphic petrology and geodynamic modeling in modern convergent orogens (Beaumont et al., 2004, 2006; England and Thompson, 1984; Thompson and England, 1984; Wang et al., 2017b). Besides, given the sedimentary protoliths on Earth's surface, formation of HP pelitic requires subduction to collision processes, because only tectonic processes related to subduction and collision can reasonably explain how the sedimentary protoliths were buried to deep crustal level (> 40 km) where they experienced HP granulite-facies metamorphism (e.g., Tam et al., 2012c; Yin et al., 2015; Zou et al., 2017). The inferred subduction and collision processes are also consistent with the defined linear distribution of HP granulites that are expected in modern convergent plate margins. Later orogenic collapse resulted in hot exhumation and cooling of the HP granulites, triggering pervasive LMP granulite-facies overprints, which eclipsed the preceding HP granulite-facies records. Therefore, any proposed tectonic models for the JLJB must consider the linear distribution of HP pelitic granulites, at least within the Jiaobei terrane, which requires geodynamic processes similar to subduction, collision and exhumation operating in modern plate tectonics. Our results thus support the opinion that the JLJB is a continental orogenic belt formed at ~1.90–1.95 Ga, coinciding with the collisional assembly of the NCC within supercontinent Columbia/Nuna (Fig. 1a; Evans and Mitchell, 2011; Rogers and Santosh, 2009; Zhai and Santosh, 2011; Zhao et al., 2002, 2004; Zhao and Zhai, 2013). The continental assembly was followed by an orogenic collapse and regional extension that resulted in exhumation and cooling of HP granulites associated with pervasive LMP granulite-facies retrograde overprints at ~1.85 Ga (Liu et al., 2013c, 2015a, 2015c, 2017a; Zou et al., 2019). It should be noted that the depositional environment intra-continent rift or magmatic arc or back-arc setting for the sedimentary protoliths of HP pelitic granulites is beyond scope of this contribution and requires further study.

8.4. Implications for Paleoproterozoic plate tectonics

When and in what form plate tectonics emerged on Earth are two fundamental questions in geology (e.g., Holder et al., 2019; Sobolev and Brown, 2019; Xu et al., 2018a), but remain greatly disputed. Metamorphic rocks from Precambrian orogenic belts are the directly accessible records of geodynamic processes in ancient Earth, and can therefore constrain the styles of plate tectonics in deep time. In this study, we show the potential for identifying kyanite relics and an earlier stage of HP granulite-facies metamorphism from typically cordierite/sillimanite-bearing LMP pelitic granulites within the Paleoproterozoic Jiao-Liao-Ji orogenic belt. This observation restores the original linear distribution of the HP pelitic granulites. The defined linear spatial distribution of HP pelitic granulites, along with the sedimentary record of Earth's surface and high-grade metamorphism at deep crustal level (> 40 km), requires Paleoproterozoic subduction and collision processes similar to modern ones. Hence, our study supports a recent hypothesis that modern plate tectonics may have been established at least since the Paleoproterozoic era (2.1–1.8 Ga), possibly on a global scale, in associated with formation of the Paleoproterozoic orogenic belts that welded supercontinent Columbia/Nuna (Fig. 1a; Xu et al., 2018a), the possible first coherent supercontinent in Earth history (Hoffman, 1989; Zhao et al., 2004). This hypothesis is primarily based on the first global records of high-pressure metamorphism with low thermal gradients (< 10 °C/km) suggestive of cold subduction, recognized from the

Paleoproterozoic tectonic belts (Ganne et al., 2012; Glassley et al., 2014; Weller and St-Onge, 2017; Xu et al., 2018a; Fig. 1a). We note these Paleoproterozoic low thermal gradients records are extremely rare in comparison to HP pelitic granulites, as four cases have been reported so far (Ganne et al., 2012; Glassley et al., 2014; Weller and St-Onge, 2017; Xu et al., 2018a). In this sense, our study provides an alternative in revealing Precambrian plate tectonics. We argue that the HP pelitic granulites can be regarded as relics of an ancient orogen (Zou et al., 2019), and their restored spatial distribution is a key in evaluating ancient geodynamic processes in comparison to the modern plate tectonics.

Notably, the rarity of Paleoproterozoic low thermal gradients has been alternatively interpreted to reflect local, anomalous subduction and collision processes similar to modern ones, but not the dominant tectonic regime during Paleoproterozoic time (Brown and Johnson, 2018; Holder et al., 2019). Global metamorphic records of the Paleoproterozoic Era are dominated by high geothermal gradients (> 15 °C/km), and mainly belong to medium to low P/T series (Brown and Johnson, 2018; Holder et al., 2019; Miyashiro, 1961). As observed here and previously (Zou et al., 2017, 2019), the apparent geothermal gradients estimated from the HP pelitic granulites within the Jiaobei terrane are 16–20 °C/km (Fig. 15), within the medium P/T series (Miyashiro, 1961), not the high P/T series as widely developed in modern plate tectonics (Brown, 2014). Similar to the interpretation of Holder et al. (2019), we suggest the higher thermal gradients and widely developed medium to low P/T series metamorphism at 2.1–1.8 Ga are due to the higher upper mantle temperatures that are thought to have existed during late Archean and Paleoproterozoic times (Herzberg et al., 2010). The higher upper mantle temperatures would produce oceanic lithosphere with greater thickness and buoyancy, because of the higher degree of decompression melting at mid-ocean ridges (Gregg et al., 2012; Keller and Schoene, 2018). Greater thickness and buoyancy of oceanic lithosphere in Paleoproterozoic time might have favored more uniformly shallow subduction (Chapman, 2017), which triggered metamorphism dominated by the medium to low P/T series. Nevertheless, shallow subduction with associated medium- to low- P/T metamorphism also exists in modern plate tectonics, as exemplified by the Pelona-Orocopia-Rand schists of southern California (Chapman, 2017). Hence, the dominant medium- to low- P/T series metamorphism cannot rule out the operation of Paleoproterozoic plate tectonics. The linear distribution of HP pelitic granulites defined in this study provides an indicator of Paleoproterozoic plate tectonics similar to modern style. The higher thermal gradient and dominant medium- to low- P/T metamorphism during Paleoproterozoic time appear to mark the difference in thermal regimes between hotter Paleoproterozoic and cooler modern subduction zones due to secular mantle cooling.

9. Conclusion

(1) Kyanite relics and the mineral assemblage of kyanite + K-feldspar + rutile + garnet are identified from typically cordierite/sillimanite-bearing LMP pelitic granulites within the Jiaobei terrane.
(2) Integrated results from petrology, pseudosection modeling, geothermobarometry, zircon and monazite geochronology suggest that these typical LMP pelitic granulites experienced an earlier HP granulite-facies metamorphism, with minimum *P-T* conditions of 860–870 °C, 13–14 kbar, possibly at ~1.95 Ga. Subsequently, these rock underwent near isothermal decompression to 4–7 kbar, > 840 °C, followed by isobaric cooling to final *P-T* conditions of ~600 °C, 4–6 kbar. The high-temperature LMP granulite-facies retrogression occurred at ~1.85 Ga that eclipsed the earlier HP granulite-facies records.
(3) At least some portions of the typically cordierite/sillimanite-bearing LMP pelitic granulites within the Jiaobei terrane are retrograded from HP pelitic granulites. This restores the original linear distribution of HP pelitic granulites.
(4) The linear distribution of HP pelitic granulites that have consistent clockwise *P-T-t* paths further supports the idea that the JLJB is a continental orogenic belt, and requires Paleoproterozoic geodynamic processes similar to subduction, collision, and exhumation operating in modern plate tectonics.

Acknowledgements

This study was supported by the National Natural Science Foundation of China (Grant Nos. 41530208 and 41890834), Chinese Acedemy of Sciences (QYZDY-SSW-DQC017), and Key Laboratory of Mineral Resources, IGGCAS (Grant No. KLMR2017-06). We are grateful to chief editor Prof. Guochun Zhao and two anonymous reviewers for their detailed and constructive comments. We thank Dr. Xiang Zhou and Hongkun Dai for kind assistance during zircon and monazite collection, Mrs. Di Zhang and Prof. Qian Mao for help with the EPMA analysis, and Prof. Xianhua Li and Qiuli Li for help with the SIMS U-Pb dating. Thoughtful discussion with Prof. Jinghui Guo is gratefully acknowledged. Finally, Yi Zou appreciates the inimitable and invaluable care and support received from his wife Dr. Xuejuan Chen. I love you.

Appendix A. Supplementary data

Supplementary data to this article can be found online at https://doi.org/10.1016/j.precamres.2020.105677.

References

Aleinikoff, J.N., Schenck, W.S., Plank, M.O., Srogi, L.A., Fanning, C.M., Kamo, S.L., Bosbyshell, H., 2006. Deciphering igneous and metamorphic events in high-grade rocks of the Wilmington Complex, Delaware: morphology, cathodoluminescence and backscattered electron zoning, and SHRIMP U-Pb geochronology of zircon and monazite. Geol. Soc. Am. Bull. 118, 39–64.
Bai, J., 1993. The Precambrian Geology and Pb-Zn Mineralization inthe Northern Margin of North China Platform. Geological Publishing House, Beijing (in Chinese).
Beaumont, C., Jamieson, R.A., Nguyen, M.H., Medvedev, S., 2004. Crustal channel flows: 1. Numerical models with applications to the tectonics of the Himalayan-Tibetan orogen. J. Geophys. Res. Solid Earth 109, 1–29.
Beaumont, C., Nguyen, M.H., Jamieson, R.A., Ellis, S., 2006. Crustal flow modes in large hot orogens. In: Law, R.D., Searle, M.P., Godin, L. (Eds.), Channel Flow, Ductile Extrusion and Exhumation in Continental Collision Zones, pp. 91–145.
Bohlen, S.R., Liotta, J.J., 1986. A barometer for garnet amphibolites and garnet granulites. J. Petrol. 27, 1025–1034.
Brown, M., 2014. The contribution of metamorphic petrology to understanding lithosphere evolution and geodynamics. Geosci. Front. 5, 553–569.
Brown, M., Johnson, T., 2018. Secular change in metamorphism and the onset of global plate tectonics. Am. Mineral. 103, 181–196.
Cai, J., Liu, F.L., Liu, P.H., Wang, F., Meng, E., Wang, W., Yang, H., Ji, L., Liu, L.S., 2017. Discovery of granulite-facies metamorphic rocks in the Ji'an area, northeastern Jiao-Liao-Ji Belt, North China Craton: metamorphic P-T evolution and geological implications. Precambr. Res. 303, 626–640.
Cawood, P.A., Hawkesworth, C.J., Dhuime, B., 2013. The continental record and the generation of continental crust. Geol. Soc. Am. Bull. 125, 14–32.
Chapman, A.D., 2017. The Pelona-Orocopia-Rand and related schists of southern California: a review of the best-known archive of shallow subduction on the planet. Int. Geol. Rev. 59, 664–701.
Cherniak, D.J., Watson, E.B., 2007. Ti diffusion in zircon. Chem. Geol. 242, 473–483.
Chowdhury, P., Chakraborty, S., 2019. Slow cooling at higher temperatures recorded within high-P Mafic granulites from the Southern Granulite Terrain, India: implications for the presence and style of plate tectonics near the archean-proterozoic boundary. J. Petrol. 60, 441–486.
Chu, H., Lu, S., Wang, H., Xiang, Z., Liu, H., 2011. U-Pb age spectrum of detrital zircons from the Fuzikuang Formation, Penglai Group in Changdao, Shandong Province. Acta Petrol. Sin. 27, 1017–1028 (in Chinese with English abstract).
Chu, X., Ague, J.J., Podladchikov, Y.Y., Tian, M., 2017. Ultrafast eclogite formation via melting-induced overpressure. Earth Planet. Sci. Lett. 479, 1–17.
Coggon, R., Holland, T.J.B., 2002. Mixing properties of phengitic micas and revised garnet-phengite thermobarometers. J. Metamorph. Geol. 20, 683–696.
Connolly, J.A.D., 2005. Computation of phase equilibria by linear programming: a tool for geodynamic modeling and its application to subduction zone decarbonation. Earth Planet. Sci. Lett. 236, 524–541.
Droop, G.T.R., 1987. A general equation for estimating Fe^{3+} concentrations in ferromagnesian silicates and oxides from microprobe analyses, using stoichiometric criteria. Mineral. Mag. 51, 431–435.
England, P.C., Thompson, A.B., 1984. Pressure temperature time paths of regional metamorphism. 1. Heat-transfer during the evolution of regions of thickened continental-crust. J. Petrol. 25, 894–928.

Evans, D.A.D., Mitchell, R.N., 2011. Assembly and breakup of the core of Paleoproterozoic-Mesoproterozoic supercontinent Nuna. Geology 39, 443–446.
Faure, M., Lin, W., Monie, P., Bruguier, O., 2004. Palaeoproterozoic arc magmatism and collision in Liaodong Peninsula (north-east China). Terra Nova 16, 75–80.
Ferry, J.M., Watson, E.B., 2007. New thermodynamic models and revised calibrations for the Ti-in-zircon and Zr-in-rutile thermometers. Contrib. Miner. Petrol. 154, 429–437.
Francois, C., Philippot, P., Rey, P., Rubatto, D., 2014. Burial and exhumation during Archean sagduction in the East Pilbara Granite-Greenstone Terrane. Earth Planet. Sci. Lett. 396, 235–251.
Fu, B., Page, F.Z., Cavosie, A.J., Fournelle, J., Kita, N.T., Lackey, J.S., Wilde, S.A., Valley, J.W., 2008. Ti-in-zircon thermometry: applications and limitations. Contrib. Miner. Petrol. 156, 197–215.
Ganne, J., De Andrade, V., Weinberg, R.F., Vidal, O., Dubacq, B., Kagambega, N., Naba, S., Baratoux, L., Jessell, M., Allibon, J., 2012. Modern-style plate subduction preserved in the Palaeoproterozoic West African craton. Nat. Geosci. 5, 60–65.
Geisler, T., Schaltegger, U., Tomaschek, F., 2007. Re-equilibration of zircon in aqueous fluids and melts. Elements 3, 43–50.
Glassley, W.E., Korstgard, J.A., Sorensen, K., Platou, S.W., 2014. A new UHP metamorphic complex in the similar to 1.8 Ga Nagssugtoqidian Orogen of West Greenland. Am. Mineral. 99, 1315–1334.
Gregg, P.M., Hebert, L.B., Montesi, L.G.J., Katz, R.F., 2012. Geodynamic models of melt generation and extraction at mid-ocean ridges. Oceanography 25, 78–88.
Harley, S.L., 1989. The origins of granulites - a metamorphic perspective. Geol. Mag. 126, 215–247.
Hermann, J., Rubatto, D., 2003. Relating zircon and monazite domains to garnet growth zones: age and duration of granulite facies metamorphism in the Val Malenco lower crust. J. Metamorph. Geol. 21, 833–852.
Herzberg, C., Condie, K., Korenaga, J., 2010. Thermal history of the earth and its petrological expression. Earth Planet. Sci. Lett. 292, 79–88.
Hoffman, P.F., 1989. Speculations on laurentia 1st gigayear (2.0 to 1.0 Ga). Geology 17, 135–138.
Holdaway, M.J., 2000. Application of new experimental and garnet Margules data to the garnet-biotite geothermometer. Am. Mineral. 85, 881–892.
Holdaway, M.J., 2001. Recalibration of the GASP geobarometer in light of recent garnet and plagioclase activity models and versions of the garnet-biotite geothermometer. Am. Mineral. 86, 1117–1129.
Holder, R.M., Viete, D.R., Brown, M., Johnson, T.E., 2019. Metamorphism and the evolution of plate tectonics. Nature. https://doi.org/10.1038/s41586-019-1462-2.
Holland, T., Baker, J., Powell, R., 1998. Mixing properties and activity-composition relationships of chlorites in the system MgO-FeO-Al_2O_3-SiO_2-H_2O. Eur. J. Mineral. 10, 395–406.
Holland, T., Powell, R., 2003. Activity-composition relations for phases in petrological calculations: an asymmetric multicomponent formulation. Contrib. Miner. Petrol. 145, 492–501.
Holland, T.J.B., Powell, R., 1998. An internally consistent thermodynamic data set for phases of petrological interest. J. Metamorph. Geol. 16, 309–343.
Indares, A., White, R.W., Powell, R., 2008. Phase equilibria modelling of kyanite-bearing anatectic paragneisses from the central Grenville Province. J. Metamorph. Geol. 26, 815–836.
Jahn, B.M., Liu, D.Y., Wan, Y.S., Song, B., Wu, J.S., 2008. Archean crustal evolution of the Jiaodong Peninsula, China, as revealed by zircon SHRIMP geochronology, elemental and Nd-isotope geochemistry. Am. J. Sci. 308, 232–269.
Jiao, S.J., Guo, J.H., Harley, S.L., Peng, P., 2013. Geochronology and trace element geochemistry of zircon, monazite and garnet from the garnetite and/or associated other high-grade rocks: implications for Palaeoproterozoic tectonothermal evolution of the Khondalite Belt, North China Craton. Precambr. Res. 237, 78–100.
Jiao, S.J., Guo, J.H., Mao, Q., Zhao, R.F., 2011. Application of Zr-in-rutile thermometry: a case study from ultrahigh-temperature granulites of the Khondalite belt, North China Craton. Contrib. Miner. Petrol. 162, 379–393.
Keller, B., Schoene, B., 2018. Plate tectonics and continental basaltic geochemistry throughout Earth history. Earth Planet. Sci. Lett. 481, 290–304.
Kelsey, D.E., Clark, C., Hand, M., 2008. Thermobarometric modelling of zircon and monazite growth in melt-bearing systems: examples using model metapelitic and metapsammitic granulites. J. Metamorph. Geol. 26, 199–212.
Kelsey, D.E., Powell, R., 2011. Progress in linking accessory mineral growth and breakdown to major mineral evolution in metamorphic rocks: a thermodynamic approach in the Na_2O-CaO-K_2O-FeO-MgO-Al_2O_3-SiO_2-H_2O-TiO_2-ZrO_2 system. J. Metamorph. Geol. 29, 151–166.
Korhonen, F.J., Brown, M., Clark, C., Bhattacharya, S., 2013. Osumilite-melt interactions in ultrahigh temperature granulites: phase equilibria modelling and implications for the P-T-t evolution of the Eastern Ghats Province, India. J. Metamorph. Geol. 31, 881–907.
Kriegsman, L.M., Alvarez-Valero, A.M., 2010. Melt-producing versus melt-consuming reactions in pelitic xenoliths and migmatites. Lithos 116, 310–320.
Kusky, T.M., Li, J.H., 2003. Paleoproterozoic tectonic evolution of the North China Craton. J. Asian Earth Sci. 22, 383–397.
Kusky, T.M., Polat, A., Windley, B.F., Burke, K.C., Dewey, J.F., Kidd, W.S.F., Maruyama, S., Wang, J.P., Deng, H., Wang, Z.S., Wang, C., Fu, D., Li, X.W., Peng, H.T., 2016. Insights into the tectonic evolution of the North China Craton through comparative tectonic analysis: a record of outward growth of Precambrian continents. Earth Sci. Rev. 162, 387–432.
Lee, Y., Cho, M., Cheong, W., Yi, K., 2018. Prolonged high-temperature, low-pressure metamorphism associated with ~1.86 Ga Sancheong-Hadong anorthosite in the Yeongnam Massif, Korea: paleoproterozoic hot orogenesis in the North China Craton. Precambr. Res. 307, 175–200.
Li, C., Li, Z., Yang, C., 2018. Palaeoproterozoic granitic magmatism in the northern segment of the Jiao-Liao-Ji Belt: implications for orogenesis along the Eastern Block of the North China Craton. Int. Geol. Rev. 60, 217–241.
Li, Q.L., Li, X.H., Lan, Z.W., Guo, C.L., Yang, Y.N., Liu, Y., Tang, G.Q., 2013. Monazite and xenotime U-Th-Pb geochronology by ion microprobe: dating highly fractionated granites at Xihuashan tungsten mine, SE China. Contrib. Miner. Petrol. 166, 65–80.
Li, S.Z., Zhao, G.C., 2007. SHRIMP U-Pb zircon geochronology of the Liaqji granitoids: constraints on the evolution of the Paleoproterozoic Jiao-Liao-Ji belt in the eastern block of the north China craton. Precambr. Res. 158, 1–16.
Li, S.Z., Zhao, G.C., Santosh, M., Liu, X., Dai, L.M., 2011. Palaeoproterozoic tectonothermal evolution and deep crustal processes in the Jiao-Liao-Ji Belt, North China Craton: a review. Geol. J. 46, 525–543.
Li, S.Z., Zhao, G.C., Santosh, M., Liu, X., Dai, L.M., Suo, Y.H., Tam, P.Y., Song, M.C., Wang, P.C., 2012. Paleoproterozoic structural evolution of the southern segment of the Jiao-Liao-Ji Belt, North China Craton. Precambr. Res. 200, 59–73.
Li, S.Z., Zhao, G.C., Sun, M., Han, Z.Z., Zhao, G.T., Hao, D.F., 2006. Are the South and North Liaohe Groups of North China Craton different exotic terranes? Nd isotope constraints. Gondwana Res. 9, 198–208.
Li, X.H., Chen, F.K., Guo, J.H., Li, Q.L., Xie, L.W., Siebel, W., 2007. South China provenance of the lower-grade Penglai Group north of the Sulu UHP orogenic belt, eastern China: evidence from detrital zircon ages and Nd-Hf isotopic composition. Geochem. J. 41, 29–45.
Li, Y.L., Zhang, H.F., Guo, J.H., Li, C.F., 2017. Petrogenesis of the Huili Paleoproterozoic leucogranite in the Jiaobei Terrane of the North China Craton: a highly fractionated albite granite forced by K-feldspar fractionation. Chem. Geol. 450, 165–182.
Li, Z., Chen, B., 2014. Geochronology and geochemistry of the Paleoproterozoic metabasalts from the Jiao-Liao-Ji Belt, North China Craton: implications for petrogenesis and tectonic setting. Precambr. Res. 255, 653–667.
Ling, X.X., Huyskens, M.H., Li, Q.L., Yin, Q.Z., Werner, R., Liu, Y., Tang, G.Q., Yang, Y.N., Li, X.H., 2017. Monazite RW-1: a homogenous natural reference material for SIMS U-Pb and Th-Pb isotopic analysis. Mineral. Petrol. 111, 163–172.
Liou, J.G., Tsujimori, T., Zhang, R.Y., Katayama, I., Maruyama, S., 2004. Global UHP metamorphism and continental subduction/collision: the Himalayan model. Int. Geol. Rev. 46, 1–27.
Liu, B., Zhai, M.G., Zhao, L., Cui, X.H., Zhou, L.G., 2019. Zircon U-Pb-Hf isotope studies of the early Precambrian metasedimentary rocks in the Kongling terrane of the Yangtze Block, South China. Precambr. Res. 320, 334–349.
Liu, F.L., Liu, L.S., Cai, J., Liu, P.H., Wang, F., Liu, C.H., Liu, J.H., 2017a. A widespread Paleoproterozoic partial melting event within the Jiao-Liao-Ji Belt, North China Craton: zircon U-Pb dating of granitic leucosomes within pelitic granulites and its tectonic implications. Precambr. Res. https://doi.org/10.1016/j.precamres.2017.10.017.
Liu, F.L., Liu, P.H., Wang, F., Liu, C.H., Cai, J., 2015a. Progresses and overviews of voluminous meta-sedimentary series within the Paleoproterozoic Jiao-Liao-Ji orogenic/mobile belt, North China Craton. Acta Petrol. Sin. 31, 2816–2846 (in Chinese with English abstract).
Liu, F.L., Liu, P.H., Wang, F., Liu, J.H., Meng, E., Cai, J., Shi, J.R., 2014. U-Pb dating of zircons from granitic leucosomes in migmatites of the Jiaobei Terrane, southwestern Jiao-Liao-Ji Belt, North China Craton: constraints on the timing and nature of partial melting. Precambr. Res. 245, 80–99.
Liu, J.H., Liu, F.L., Ding, Z.J., Liu, C.H., Yang, H., Liu, P.H., Wang, F., Meng, E., 2013a. The growth, reworking and metamorphism of early Precambrian crust in the Jiaobei terrane, the North China Craton: constraints from U-Th-Pb and Lu-Hf isotopic systematics, and REE concentrations of zircon from Archean granitoid gneisses. Precambr. Res. 224, 287–303.
Liu, J.H., Liu, F.L., Ding, Z.J., Liu, P.H., Wang, F., 2015b. Early Precambrian major magmatic events, and growth and evolution of continental crust in the Jiaobei terrane, North China Craton. Acta Petrol. Sin. 31, 2942–2958 (in Chinese with English abstract).
Liu, J.H., Liu, F.L., Ding, Z.J., Yang, H., Liu, C.H., Liu, P.H., Xiao, L.L., Zhao, L., Geng, J.Z., 2013b. U-Pb dating and Hf isotope study of detrital zircons from the Zhifu Group, Jiaobei Terrane, North China Craton: provenance and implications for Precambrian crustal growth and recycling. Precambr. Res. 235, 230–250.
Liu, J.H., Liu, F.L., Liu, P.H., Wang, F., Ding, Z.J., 2011a. Polyphase magmatic and metamorphic events from Early Precambrian metamorphic basement in Jiaobei area: evidences from the zircon U-Pb dating of TTG and granitic gneisses. Acta Petrol. Sin. 27, 943–960 (in Chinese with English abstract).
Liu, P.H., Cai, J., Wang, F., Liu, C.H., Liu, J.H., Yang, H., Shi, J.R., Liu, L.S., 2017b. Discovery and geological significance of high-pressure mafic granulites in the Pingdu-Anqiu area of the Jiaobei Terrane, the Jiao-Liao-Ji Belt, the North China Craton. Precambr. Res. 303, 445–469.
Liu, P.H., Liu, F.L., Liu, C.H., Wang, F., Liu, J.H., Yang, H., Cai, J., Shi, J.R., 2013c. Petrogenesis, P-T-t path, and tectonic significance of high-pressure mafic granulites from the Jiaobei terrane, North China Craton. Precambr. Res. 233, 237–258.
Liu, P.H., Liu, F.L., Wang, F., Liu, C.H., Yang, H., Liu, J.H., Cai, J., Shi, J.R., 2015c. P-T-t paths of the multiple metamorphic events of the Jiaobei terrane in the southeastern segment of the Jiao-Liao-Ji Belt (JLJB), in the North China Craton: implication for formation and evolution of the JLJB. Acta Petrol. Sin. 31, 2889–2941 (in Chinese with English abstract).
Liu, P.H., Liu, F.L., Wang, F., Liu, J.H., 2011b. U-Pb dating of zircons from Al-rich paragneisses of Jinshan Group in Shandong peninsula and its geological significance. Acta Petrologica et Mineralogica 829–843 (in Chinese with English abstract).
Lu, L.Z., Jin, S.Q., 1993. P-T-t paths and tectonic history of an early Precambrian granulite-facies terrane, Jining district, south-east inner-Mongolia, China. J. Metamorph. Geol. 11, 483–498.
Lu, L.Z., Xu, X.C., Liu, F.L., 1996. Early Precambrian Khondalites in North China. Jilin Science and Technology Press (in Chinese), Changchun.

Ludwig, K.R., 2012. User's Manual for Isoplot 3.75: A Geochronological Toolkit for Microsoft Excel. Berkeley Geochronology Centre Special Publication.
Luo, Y., Sun, M., Zhao, G.C., Li, S.Z., Ayers, J.C., Xia, X.P., Zhang, J.H., 2008. A comparison of U-Pb and Hf isotopic compositions of detrital zircons from the North and South Liaohe Groups: constraints on the evolution of the Jiao-Liao-Ji Belt, North China Craton. Precambr. Res. 163, 279–306.
Luo, Y., Sun, M., Zhao, G.C., Li, S.Z., Xu, P., Ye, K., Xia, X.P., 2004. LA-ICP-MS U-Pb zircon ages of the Liaohe Group in the Eastern Block of the North China Craton: constraints on the evolution of the Jiao-Liao-Ji Belt. Precambr. Res. 134, 349–371.
Meinhold, G., 2010. Rutile and its applications in earth sciences. Earth Sci. Rev. 102, 1–28.
Meng, E., Liu, F.L., Liu, P.H., Liu, C.H., Yang, H., Wang, F., Shi, J.R., Cai, J., 2014. Petrogenesis and tectonic significance of Paleoproterozoic meta-mafic rocks from central Liaodong Peninsula, northeast China: evidence from zircon U-Pb dating and in situ Lu-Hf isotopes, and whole-rock geochemistry. Precambr. Res. 247, 92–109.
Miyashiro, A., 1961. Evolution of metamorphic belts. J. Petrol. 2, 277–311.
O'Brien, P.J., Rotzler, J., 2003. High-pressure granulites: formation, recovery of peak conditions and implications for tectonics. J. Metamorph. Geol. 21, 3–20.
Palin, R.M., Weller, O.M., Waters, D.J., Dyck, B., 2016. Quantifying geological uncertainty in metamorphic phase equilibria modelling; a Monte Carlo assessment and implications for tectonic interpretations. Geosci. Front. 7, 591–607.
Pauly, J., Marschall, H.R., Meyer, H.P., Chatterjee, N., Monteleone, B., 2016. Prolonged Ediacaran-Cambrian metamorphic history and short-lived high-pressure granulite-facies metamorphism in the HU Sverdrupfjella, Dronning Maud Land (East Antarctica): evidence for Continental Collision during Gondwana Assembly. J. Petrol. 57, 185–227.
Peng, C., Xue, L.F., Zhu, M., Chai, Y., Liu, W.Y., 2016. The location and evolution of the tectonic boundary between the Paleoproterozoic Jiao-Liao-Ji Belt and the Longgang Block, northeast China. Precambr. Res. 272, 18–38.
Peng, P., Wang, X.P., Windley, B.F., Guo, J.H., Zhai, M.G., Li, Y., 2014. Spatial distribution of similar to 1950–1800 Ma metamorphic events in the North China Craton: implications for tectonic subdivision of the craton. Lithos 202, 250–266.
Prakash, D., 1999. Cordierite-bearing gneisses from Kodaikanal, South India: textural relationship and P-T conditions. J. Geol. Soc. India 54, 347–358.
Rogers, J.J.W., Santosh, M., 2009. Tectonics and surface effects of the supercontinent Columbia. Gondwana Res. 15, 373–380.
Rubatto, D., Hermann, J., 2006. Zircon/garnet trace element partitioning: a tool for P-T-time paths. Geochimica Et Cosmochimica Acta 70, A542.
Rubatto, D., Hermann, J., Buick, I.S., 2006. Temperature and bulk composition control on the growth of monazite and zircon during low-pressure anatexis (Mount Stafford, central Australia). J. Petrol. 47, 1973–1996.
Schaltegger, U., Fanning, C.M., Gunther, D., Maurin, J.C., Schulmann, K., Gebauer, D., 1999. Growth, annealing and recrystallization of zircon and preservation of monazite in high-grade metamorphism: conventional and in-situ U-Pb isotope, cathodoluminescence and microchemical evidence. Contrib. Miner. Petrol. 134, 186–201.
Schmalholz, S.M., Podladchikov, Y.Y., 2013. Tectonic overpressure in weak crustal-scale shear zones and implications for the exhumation of high-pressure rocks. Geophys. Res. Lett. 40, 1984–1988.
Siegel, C., Bryan, S.E., Allen, C.M., Gust, D.A., 2018. Use and abuse of zircon-based thermometers: a critical review and a recommended approach to identify antecrystic zircons. Earth Sci. Rev. 176, 87–116.
Slama, J., Kosler, J., Condon, D.J., Crowley, J.L., Gerdes, A., Hanchar, J.M., Horstwood, M.S.A., Morris, G.A., Nasdala, L., Norberg, N., Schaltegger, U., Schoene, B., Tubrett, M.N., Whitehouse, M.J., 2008. Plesovice zircon - a new natural reference material for U-Pb and Hf isotopic microanalysis. Chem. Geol. 249, 1–35.
Sobolev, S.V., Brown, M., 2019. Surface erosion events controlled the evolution of plate tectonics on Earth. Nature 570, 52–57.
Spear, F.S., Kohn, M.J., Cheney, J.T., 1999. P-T paths from anatectic pelites. Contrib. Miner. Petrol. 134, 17–32.
Sun, S.S., Mcdonough, W.F., 1989. Chemical and isotopic systematics of oceanic basalts: Implications for mantle composition and processe. Special Publications In: Saunders, A.D., Norry, M.J. (Eds.), Magmatism in the Ocean Basins. Geological Society, London, pp. 313–345.
Tam, P.Y., Zhao, G.C., Liu, F.L., Zhou, X.W., Sun, M., Li, S.Z., 2011. Timing of metamorphism in the Paleoproterozoic Jiao-Liao-Ji Belt: new SHRIMP U-Pb zircon dating of granulites, gneisses and marbles of the Jiaobei massif in the North China Craton. Gondwana Res. 19, 150–162.
Tam, P.Y., Zhao, G.C., Sun, M., Li, S.Z., Iizuka, Y., Ma, G.S.K., Yin, C.Q., He, Y.H., Wu, M.L., 2012a. Metamorphic P-T path and tectonic implications of medium-pressure pelitic granulites from the Jiaobei massif in the Jiao-Liao-Ji Belt, North China Craton. Precambr. Res. 220, 177–191.
Tam, P.Y., Zhao, G.C., Sun, M., Li, S.Z., Wu, M.L., Yin, C.Q., 2012b. Petrology and metamorphic P-T path of high-pressure mafic granulites from the Jiaobei massif in the Jiao-Liao-Ji Belt, North China Craton. Lithos 155, 94–109.
Tam, P.Y., Zhao, G.C., Zhou, X.W., Sun, M., Guo, J.H., Li, S.Z., Yin, C.Q., Wu, M.L., He, Y.H., 2012c. Metamorphic P-T path and implications of high-pressure pelitic granulites from the Jiaobei massif in the Jiao-Liao-Ji Belt, North China Craton. Gondwana Res. 22, 104–117.
Tang, J., Zheng, Y.F., Wu, Y.B., Gong, B., Liu, X.M., 2007. Geochronology and geochemistry of metamorphic rocks in the Jiaobei terrane: constraints on its tectonic affinity in the Sulu orogen. Precambr. Res. 152, 48–82.
Thompson, A.B., England, P.C., 1984. Pressure temperature time paths of regional metamorphism. 2. Their inference and interpretation using mineral assemblages in metamorphic rocks. J. Petrol. 25, 929–955.
Tian, Z.H., Liu, F.L., Windley, B.F., Liu, P.H., Wang, F., Liu, C.H., Wang, W., Cai, J., Xiao, W.J., 2017. Polyphase structural deformation of low- to medium-grade metamorphic rocks of the Liaohe Group in the Jiao-Liao-Ji Orogenic Belt, North China Craton: correlations with tectonic evolution. Precambr. Res. 303, 641–659.
Tomkins, H.S., Powell, R., Ellis, D.J., 2007. The pressure dependence of the zirconium-in-rutile thermometer. J. Metamorph. Geol. 25, 703–713.
Trap, P., Faure, M., Lin, W., Monie, P., 2007. Late Paleoproterozoic (1900–1800 Ma) nappe stacking and polyphase deformation in the Hengshan-Wutaishan area: implications for the understanding of the Trans-North-China belt, North China Craton. Precambr. Res. 156, 85–106.
Tucker, N.M., Hand, M., Payne, J.L., 2015. A rift-related origin for regional medium-pressure, high-temperature metamorphism. Earth Planet. Sci. Lett. 421, 75–88.
Turkina, O.M., Sukhorukov, V.P., 2015. Early Precambrian high-grade metamorphosed terrigenous rocks of granulite-gneiss terranes of the Sharyzhalgai uplift (south-western Siberian craton). Russ. Geol. Geophys. 56, 874–884.
Vavra, G., Gebauer, D., Schmid, R., Compston, W., 1996. Multiple zircon growth and recrystallization during polyphase Late Carboniferous to Triassic metamorphism in granulites of the Ivrea Zone (Southern Alps): an ion microprobe (SHRIMP) study. Contrib. Miner. Petrol. 122, 337–358.
Wan, B., Windley, B.F., Xiao, W.J., Feng, J.Y., Zhang, J., 2015. Paleoproterozoic high-pressure metamorphism in the northern North China Craton and implications for the Nuna supercontinent. Nat. Commun. 6, 1–10.
Wang, F., Liu, F.L., Liu, P.H., Cai, J., Schertl, H.P., Ji, L., Liu, L.S., Tian, Z.H., 2017a. In situ zircon U-Pb dating and whole-rock geochemistry of metasedimentary rocks from South Liaohe Group, Jiao-Liao-Ji orogenic belt: constraints on the depositional and metamorphic ages, and implications for tectonic setting. Precambr. Res. 303, 764–780.
Wang, F., Liu, F.L., Liu, P.H., Liu, J.H., 2010. Metamorphic evolution of Early Precambrian khondalite series in North Shandong Province. Acta Petrol. Sin. 26, 2057–2072 (in Chinese with English abstract).
Wang, J.M., Wu, F.Y., Rubatto, D., Liu, S.R., Zhang, J.J., Liu, X.C., Yang, L., 2017b. Monazite behaviour during isothermal decompression in pelitic granulites: a case study from Dinggye, Tibetan Himalaya. Contrib. Miner. Petrol. 172, 1–30.
Wang, M.J., Liu, S.W., Fu, J.H., Wang, K., Guo, R.R., Guo, B.R., 2017c. Neoarchean DTTG gneisses in southern Liaoning Province and their constraints on crustal growth and the nature of the Liao-Ji Belt in the Eastern Block. Precambr. Res. 303, 187–207.
Wang, P.C., 1995. Relationships between the Jingshan Group and the Fenzishan Group in the Jiaobei area. Regional Geol. China 1, 15–20 (in Chinese with English abstract).
Wang, W., Zhai, M.G., Li, T.S., Santosh, M., Zhao, L., Wang, H.Z., 2014. Archean-Paleoproterozoic crustal evolution in the eastern North China Craton: zircon U-Th-Pb and Lu-Hf evidence from the Jiaobei terrane. Precambr. Res. 241, 146–160.
Waters, D.J., 2001. The significance of prograde and retrograde quartz-bearing intergrowth microstructures in partially melted granulite-facies rocks. Lithos 56, 97–110.
Watson, E.B., Wark, D.A., Thomas, J.B., 2006. Crystallization thermometers for zircon and rutile. Contrib. Miner. Petrol. 151, 413–433.
Wei, C.J., 2016. Granulite facies metamorphism and petrogenesis of granite (II): quantitative modeling of the HT-UHT phase equilibria for metapelites and the petrogenesis of S-type granite. Acta Petrol. Sin. 32, 1625–1643 (in Chinese with English abstract).
Weller, O.M., St-Onge, M.R., 2017. Record of modern-style plate tectonics in the Palaeoproterozoic Trans-Hudson orogen. Nat. Geosci. 10, 305–313.
White, R.W., Powell, R., Clarke, G.L., 2002. The interpretation of reaction textures in Fe-rich metapelitic granulites of the Musgrave Block, central Australia: constraints from mineral equilibria calculations in the system K_2O-FeO-MgO-Al_2O_3-SiO_2-H_2O-TiO_2-Fe_2O_3. J. Metamorph. Geol. 20, 41–55.
White, R.W., Powell, R., Holland, T.J.B., 2007. Progress relating to calculation of partial melting equilibria for metapelites. J. Metamorph. Geol. 25, 511–527.
White, R.W., Powell, R., Holland, T.J.B., Worley, B.A., 2000. The effect of TiO_2 and Fe_2O_3 on metapelitic assemblages at greenschist and amphibolite facies conditions: mineral equilibria calculations in the system K_2O-FeO-MgO-Al_2O_3-SiO_2-H_2O-TiO_2-Fe_2O_3. J. Metamorph. Geol. 18, 497–511.
Whitney, D.L., Evans, B.W., 2010. Abbreviations for names of rock-forming minerals. Am. Mineral. 95, 185–187.
Wickham, S.M., Oxburgh, E.R., 1985. Continental Rifts as a Setting for Regional Metamorphism. Nature 318, 330–333.
Wiedenbeck, M., Hanchar, J.M., Peck, W.H., Sylvester, P., Valley, J., Whitehouse, M., Kronz, A., Morishita, Y., Nasdala, L., Fiebig, J., Franchi, I., Girard, J.P., Greenwood, R.C., Hinton, R., Kita, N., Mason, P.R.D., Norman, M., Ogasawara, M., Piccoli, R., Rhede, D., Satoh, H., Schulz-Dobrick, B., Skar, O., Spicuzza, M.J., Terada, K., Tindle, A., Togashi, S., Vennemann, T., Xie, Q., Zheng, Y.F., 2004. Further characterisation of the 91500 zircon crystal. Geostand. Geoanal. Res. 28, 9–39.
Williams, I.S., 1998. U-Th-Pb geochronology by ion microprobe. In: McKibben, M.A., Shanks, W.C., Ridley, W.I. (Eds.), Applications of Microanalytical Techniques to Understanding Mineralizing Processes. Reviews in Economic Geology. Society of Economic Geologists, El Paso, pp. 1–35.
Wu, J.L., Zhang, H.F., Zhai, M.G., Guo, J.H., Liu, L., Yang, W.Q., Wang, H.Z., Zhao, L., Jia, X.L., Wang, W., 2016. Discovery of pelitic high-pressure granulite from Manjinggou of the Huai'an Complex, North China Craton: metamorphic P-T evolution and geological implications. Precambr. Res. 278, 323–336.
Wu, M.L., Zhao, G.C., Sun, M., Li, S.Z., Bao, Z.A., Tam, P.Y., Eizenhoefer, P.R., He, Y.H., 2014. Zircon U-Pb geochronology and Hf isotopes of major lithologies from the Jiaodong Terrane: implications for the crustal evolution of the Eastern Block of the North China Craton. Lithos 190, 71–84.
Wu, Y.B., Gao, S., Zhang, H.F., Yang, S.H., Jiao, W.F., Liu, Y.S., Yuan, H.L., 2008. Timing of UHP metamorphism in the Hong'an area, western Dabie Mountains, China: evidence from zircon U-Pb age, trace element and Hf isotope composition. Contrib. Miner. Petrol. 155, 123–133.
Xie, L.W., Zhang, Y.B., Zhang, H.H., Sun, J.F., Wu, F.Y., 2008. In situ simultaneous

determination of trace elements, U-Pb and Lu-Hf isotopes in zircon and baddeleyite. Chin. Sci. Bull. 53, 1565–1573.
Xu, C., Kynicky, J., Song, W.L., Tao, R.B., Lu, Z., Li, Y.X., Yang, Y.C., Pohanka, M., Galiova, M.V., Zhang, L.F., Fei, Y.W., 2018a. Cold deep subduction recorded by remnants of a Paleoproterozoic carbonated slab. Nat. Commun. 9, 1–8.
Xu, W., Liu, F.L., 2019. Geochronological and geochemical insights into the tectonic evolution of the Paleoproterozoic Jiao-Liao-Ji Belt, Sino-Korean Craton. Earth Sci. Rev. 193, 162–198.
Xu, W., Liu, F.L., Tian, Z.H., Liu, L.S., Ji, L., Dong, Y.S., 2018b. Source and petrogenesis of Paleoproterozoic meta-mafic rocks intruding into the North Liaohe Group: implications for back-arc extension prior to the formation of the Jiao-Liao-Ji Belt, North China Craton. Precambr. Res. 307, 66–81.
Yan, Y.H., Zhai, M.G., Guo, J.H., 1991. The cordierite-sillimanite assemblages in the Archean granulite belt on North China Platform as an indicator for low-pressure granulite facies. Acta Petrol. Sin. 4, 47–56 (in Chinese with English abstract).
Yang, C.W., Liu, J.L., Yang, H.X., Zhang, C., Feng, J., Lu, T.J., Sun, Y.Q., Zhang, J., 2019. Tectonics of the Paleoproterozoic Jiao-Liao-Ji orogenic belt in the Liaodong peninsula, North China Craton: a review. J. Asian Earth Sci. 176, 141–156.
Yin, C.Q., Zhao, G.C., Sun, M., 2015. High-pressure pelitic granulites from the Helanshan Complex in the Khondalite Belt, North China Craton: metamorphic P-T path and tectonic implications. Am. J. Sci. 315, 846–879.
Yuan, L.L., Zhang, X.H., Xue, F.H., Han, C.M., Chen, H.H., Zhai, M.G., 2015. Two episodes of Paleoproterozoic mafic intrusions from Liaoning province, North China Craton: petrogenesis and tectonic implications. Precambr. Res. 264, 119–139.
Zack, T., Moraes, R., Kronz, A., 2004. Temperature dependence of Zr in rutile: empirical calibration of a rutile thermometer. Contrib. Miner. Petrol. 148, 471–488.
Zhai, M.G., 2009. Two kinds of granulites (HT-HP and HT-UHT) in North China Craton: their genetic relation and geotectonic implications. Acta Petrol. Sin. 25, 1753–1771 (in Chinese with English abstract).
Zhai, M.G., Liu, W.J., 2003. Palaeoproterozoic tectonic history of the North China craton: a review. Precambr. Res. 122, 183–199.
Zhai, M.G., Santosh, M., 2011. The early Precambrian odyssey of the North China Craton: a synoptic overview. Gondwana Res. 20, 6–25.
Zhang, Q.S., 1984. Geology and Metallogeny of the Early Precambrian in China. Jinlin People's Publishing House, Changchun, pp. 66–70 (in Chinese).
Zhang, Q.S., Yang, Z.S., 1988. In: Early Crust and Mineral Deposits of Liaodong Peninsula, China. Geological Publishing House, Beijing, pp. 1–575 (in Chinese).
Zhang, W., Liu, F.L., Cai, J., Liu, C.H., Liu, J.H., Liu, P.H., Liu, L.S., Wang, F., Yang, H., 2018. Geochemistry, zircon U-Pb dating and tectonic implications of the Palaeoproterozoic Ji'an and Laoling groups, northeastern Jiao-Liao-Ji Belt, North China Craton. Precambr. Res. 314, 264–287.
Zhao, G.C., Cawood, P.A., Wilde, S.A., Lu, L.Z., 2001. High-pressure granulites (retrogaded eclogites) from the Hengshan Complex, North China Craton: petrology and tectonic implications. J. Petrol. 42, 1141–1170.
Zhao, G.C., Cawood, P.A., Wilde, S.A., Sun, M., 2002. Review of global 2.1-1.8 Ga orogens: implications for a pre-Rodinia supercontinent. Earth Sci. Rev. 59, 125–162.
Zhao, G.C., Sun, M., Wilde, S.A., Li, S.Z., 2004. A Paleo-Mesoproterozoic supercontinent: assembly, growth and breakup. Earth Sci. Rev. 67, 91–123.
Zhao, G.C., Sun, M., Wilde, S.A., Li, S.Z., 2005. Late Archean to Paleoproterozoic evolution of the North China Craton: key issues revisited. Precambr. Res. 136, 177–202.
Zhao, G.C., Zhai, M.G., 2013. Lithotectonic elements of Precambrian basement in the North China Craton: review and tectonic implications. Gondwana Res. 23, 1207–1240.
Zhao, L., Li, T.S., Peng, P., Guo, J.H., Wang, W., Wang, H.Z., Santosh, M., Zhai, M.G., 2015. Anatomy of zircon growth in high pressure granulites: SIMS U-Pb geochronology and Lu-Hf isotopes from the Jiaobei Terrane, eastern North China Craton. Gondwana Res. 28, 1373–1390.
Zhou, J.B., Wilde, S.A., Zhao, G.C., Zheng, C.Q., Jin, W., Zhang, X.Z., Cheng, H., 2008a. SHRIMP U-Pb zircon dating of the Neoproterozoic Penglai Group and Archean gneisses from the Jiaobei Terrane, North China, and their tectonic implications. Precambr. Res. 160, 323–340.
Zhou, L.G., Zhai, M.G., Lu, J.S., Zhao, L., Wang, H.Z., Wu, J.L., Liu, B., Zou, Y., Shan, H.X., Cui, X.H., 2017. Paleoproterozoic metamorphism of high-grade granulite facies rocks in the North China Craton: study advances, questions and new issues. Precambr. Res. 303, 520–547.
Zhou, X.W., Wei, C.J., Geng, Y.S., Zhang, L.F., 2004. Discovery and implications of the high-pressure pelitic granulite from the Jiaobei massif. Chin. Sci. Bull. 49, 1942–1948.
Zhou, X.W., Zhao, G.C., Wei, C.J., Geng, Y.S., Sun, M., 2008b. EPMA, U-Th-Pb monazite and SHRIMP U-Pb zircon geochronology of high-pressure pelitic granulites in the Jiaobei massif of the North China Craton. Am. J. Sci. 308, 328–350.
Zou, Y., Zhai, M., Santosh, M., Zhou, L., Zhao, L., Lu, J., Shan, H., 2017. High-pressure pelitic granulites from the Jiao-Liao-Ji Belt, North China Craton: a complete P-T path and its tectonic implications. J. Asian Earth Sci. 134, 103–121.
Zou, Y., Zhai, M.G., Santosh, M., Zhou, L.G., Zhao, L., Lu, J.S., Liu, B., Shan, H.X., 2018. Contrasting P-T-t paths from a Paleoproterozoic metamorphic orogen: petrology, phase equilibria, zircon and monazite geochronology of metapelites from the Jiao-Liao-Ji belt, North China Craton. Precambr. Res. 311, 74–97.
Zou, Y., Zhai, M.G., Zhou, L.G., Zhao, L., Lu, J.S., Wang, Y.Q., Shan, H.X., 2019. Relics of a Paleoproterozoic orogen: New petrological, phase equilibria and geochronological studies on high-pressure pelitic granulites from the Pingdu-Laiyang areas, southwest of the Jiaobei terrane, North China Craton. Precambr. Res. 322, 136–159.